Eph-Ephrin Tetramerization Inhibitors Target Bidirectional Signaling to Combat Pain and Addiction

Hanghang Wang[1], Amav Khambete[1], Frances Sprouse, Melody Karsi, Karina Cortez, Eric Bellinghausen, Tamdan Khuu, Natalie Block, Asghar Talebian[2], Mahmoud Salama Ahmed[3], Chinthaka Mahesh Udamulle Gedara, Michael Ortiz, & Mark Henkemeyer*

Affiliation

Department of Neuroscience, Kent Waldrep Foundation Center for Basic Research on Nerve Growth and Regeneration, Peter O'Donnell Jr. Brain Institute, University of Texas Southwestern Medical Center, Dallas, TX 75390, USA

[1]Equal first authors

[2]Current affiliation: Department of Pathology and Genomic Medicine, Houston Methodist Hospital, Houston, Texas 77030, USA

[3]Current affiliation: Department of Pharmaceutical Sciences, Texas Tech University Health Sciences Center, Amarillo, Texas 79106, USA

*Corresponding author: Email: mark.henkemeyer@utsouthwestern.edu

Summary

Ephs and Ephrins are highly conserved membrane-anchored proteins that form dimers, tetramers, and tetramer superclusters upon cell-cell contact to become activated and transduce powerful bidirectional phosphotyrosine signals into the cells they are expressed on. While most noted for their roles in development and neuronal pathfinding, Eph/Ephrin molecules are now recognized to become overexpressed and signal excessively in numerous unmet medical conditions, including chronic pain, fibroinflammatory disorders, and cancer. We searched for small molecules that inhibit Eph-Ephrin interactions and discovered compounds with submicromolar activity that specifically target the high-affinity circular tetramer structure necessary for activation of signal transduction by these molecules. Eph-Ephrin tetramer inhibitors are orally available, exhibit drug-like qualities to reduce both Eph forward and Ephrin reverse signaling, and act to blunt chronic pain and opioid withdrawal behaviors. Tetramer inhibitors thus present a novel approach to target Eph-Ephrin macromolecular interactions and counter chronic conditions caused or exacerbated by excessive bidirectional signaling.

Introduction

Studies of the Eph family receptor tyrosine kinases and their cognate Ephrin ligands have posed many challenges over the years[1,2]. This is because there are 14 different receptors and 8 different ligands, all membrane-attached, that promiscuously interact upon cell-cell contact to form dimers, tetramers, and tetramer super-clusters[3], which then become activated to transduce bidirectional phosphotyrosine-mediated signals into both the Eph-expressing cell (forward signaling) and Ephrin-expressing cell (reverse signaling) (Fig. 1a)[4-6]. While early discoveries revealed developmental roles in axon pathfinding, cell migration, and vascular development, Ephs and Ephrins are also thought to regulate tissue homeostasis in the adult, most notably in stem cells and neural plasticity[7,8].

Much evidence implicates dysregulated Eph/Ephrin expression and signaling in pathology, including cancer biology, where these molecules can influence proliferation, migration, metastasis, and tumor angiogenesis[9]. They are also implicated in multiple chronic inflammatory/fibrotic/autoimmune type diseases and metabolic disorders, where overexpression of select molecules strongly correlates with disease progression[10]. A direct role for EphB2 and EphrinB2 in causing the pathology of fibroinflammatory disorders is revealed by studies that show knockout/knockdown of

either the receptor or the ligand protect the animal from developing fibrosis in numerous tissues including models of skin (scleroderma), kidney (chronic kidney disease), and heart (myocardial infarction) fibrosis[11-14]. Liver fibrosis caused by metabolic dysfunction-associated steatohepatitis (MASH) is another example of EphB2 involvement in fibroinflammatory disorders. We show in the accompanying manuscript that EphB2 is required for the development of diet-induced liver fibrosis[15], a role consistent with reports this receptor becomes progressively overexpressed in the livers of patients with fatty liver disease and MASH[16-18]. The pathological roles for Ephs and Ephrins may be related to wound healing gone awry[10]; in the normal uninjured situation, expression of Eph/Ephrin in adult tissues and cells is typically in a quiescent low state, whereas following injury, whatever the cause may be (high blood pressure, heart attack, high fat diet), the cells in the injured tissue attempt to repair the damage by reverting to the embryonic program of high Eph/Ephrin expression. This leads to excessive Eph-Ephrin interactions and signaling which is counterproductive and can result in pathological consequences.

Dysregulated Eph/Ephrin expression and signaling is also associated with several neurological disorders, including Alzheimer's disease, multiple sclerosis, ischemic stroke and neuroinflammation, spinal cord injury, opioid dependency, and chronic pain[19]. The EphB1 and EphB2 receptor tyrosine kinases in particular have emerged as key synaptic signaling molecules that become overexpressed in chronic pain[20]. EphB2 signals in primary sensory nociceptors by interacting with Ephrin ligands in peripheral target tissues[21,22], while EphB1 becomes overexpressed and signals in the dorsal horn (DH) neurons within the spinal cord by interacting with centrally-projecting nociceptor pre-synaptic fibers from the dorsal root ganglion (DRG) that express EphrinB2[23-28]. In both cases, the activated post-synaptic localized EphB receptor physically associates with and induces tyrosine phosphorylation of the N-methyl-D-aspartate receptor (NMDAR)[29,30], allowing calcium influx to activate nociceptors (EphB2) and DH neurons (EphB1). This strengthens DH synapses (long-term potentiation, LTP), and results in central sensitization and feelings of chronic pain. People with rheumatoid arthritis show increased synovial fibroblast expression of *EPHRINA3* (*EFNA3*)[31], *EPHRINA5* (*EFNA5*)[32], and *EPHRINB1* (*EFNB1*)[33], those with diabetic neuropathic pain show upregulated *EPHRINB3* (*EFNB3*) in the DRG[34], and *EPHRINB2* (*EFNB2*) was recently shown to be one of the most significantly overexpressed DRG genes in patients with cervical neuropathic pain[35]. This new human information is very important as nociceptor-specific conditional knockout of *EphrinB2* showed the crucial role of this ligand in inflammatory and neuropathic pain[26].

EphB1-/- homozygous knockout (KO) mice, even *EphB1*-/-;*EphB2*-/-;*EphB3*-/- triple KO mice, are viable long-lived unremarkable appearing animals that exhibit normal feelings of acute pain needed for day-to-day activities and survival[36]. Remarkably, when *EphB1* KO mice were subjected to various chronic pain-generating nerve injury models, they did not develop enhanced pain sensitivity like their wild-type (WT) counterparts[23,27,28], nor did they generate spinal LTP needed for central sensitization[25]. This indicates EphB1 receptor signaling is central to the development of chronic pain. Even *EphB1* +/- heterozygous mice are refractory to developing neuropathic pain[23]. This suggests a pharmacological strategy to target this receptor would only need to reduce its expression/signaling 50%. Further, our new studies indicate EphrinB2 reverse signaling is also important for chronic pain, especially the early, intense feelings immediately after injury (see below). Being that both forward and reverse signaling likely participate in chronic pain, we searched for compounds that interfere with the ability of EphB1 to bind EphrinB2 as a traditional approach to identify an EphB1 kinase inhibitor[37] would fail to counter pathological EphrinB2 reverse signaling. Our goal, therefore, was to identify compounds that interfere with both EphB forward and EphrinB reverse signaling.

Results

EphB-EphrinB binding kinetics

Commercially available soluble epitope-tagged ectodomains of various mammalian Eph and Ephrin proteins were obtained and tested using biophysical methods to visualize their binding interactions in real-time using biolayer interferometry (BLI). Shown in Fig 1b are experiments in which human EphrinB1-Fc, EphrinB2-Fc, and EphrinB3-Fc ectodomain proteins were sparsely immobilized onto AHC biosensor chips and then, after baseline measurements, exposed to 50 nM of soluble human EphB1-His, EphB2-His, and EphB4-His ectodomains for an 800 sec association step followed by a 1,000 sec dissociation step. The response data displayed in the sensorgrams clearly shows EphB1 and EphB2 receptors promiscuously interacted with all three EphrinB proteins, whereas cardiovascular-specific EphB4, bound only to EphrinB2 as expected. Notably, all three EphB ectodomains exhibited the strongest binding to EphrinB2, with the EphB4 sensorgram showing the fastest/strongest binding with a very steep response slope and with binding nearly complete within the first 200 sec of association at which point the response quickly flattened. In contrast, the binding of EphB1 and EphB2 to immobilized EphrinB2 occurred more slowly and with

no sign of the response slope reaching a plateau, even at the end of the 800 sec association step. Once placed into dissociation, all three EphB-EphrinB2 interactions exhibited similar profiles with a fair amount of EphB protein coming off the EphrinB2-bound sensorchips, though ~50% or more of the respective receptor protein remained bound at the end of the 1,000 sec dissociation step. This indicates formation of very stable, long-lasting macromolecular protein complexes (tetramers). To confirm the EphrinB2-EphB interactions, we biotinylated and immobilized rat EphB1-Fc, mouse EphB2-Fc, and mouse EphB4-Fc ectodomains onto SSA sensorchips and assessed for binding to 10, 30, and 100 nM soluble mouse EphrinB2-His ectodomain (Fig. 1c), and also immobilized biotinylated mouse EphrinB2-His onto SSA sensor chips and assessed for binding to 1, 30, and 100 nM soluble rat EphB1-Fc ectodomain (Extended Data Fig. 1a). All produced similar binding curves irrespective of which protein was immobilized onto the sensor chip or whether human or rodent derived proteins were used.

Consistent with their known abilities to form dimers and tetramers, the binding kinetics and curve fits for the above three EphB-EphrinB2 interactions indicate formation of very high affinity and complex 2:1 type heterologous interactions as opposed to simple 1:1 dimer interactions (Extended Data Fig. 1). With 2:1 type interactions, two K_D values are calculated, in our case K_{D2} to describe dimer formation and K_{D1} to describe tetramer formation. BLI runs using multiple concentrations of the soluble component provide for most accurate global fit calculations and confirm the very high tetramer affinities of the three different EphB-EphrinB2 interactions fall in a 0.28-6 nM range and with dimer affinities in the 15-80 nM range (Fig. 1c and Extended Data Fig. 1), similar to earlier reports using surface plasmon resonance[38].

EphrinB1 and EphrinB3 ectodomains also exhibited low/sub nanomolar binding affinities with EphB1 and EphB2, though here complex formation between the proteins was different from EphrinB2 (Fig. 1b and Extended Data Fig. 1b,d). EphB1-EphrinB1, EphB1-EphrinB3, and EphB2-EphrinB3 all showed very slow binding in the association step with straight slopes, without any sign of response plateauing, and with no loss of receptor binding in the dissociation step. This indicates these proteins assemble directly into very high affinity tetramers, apparently bypassing the need for dimer formation. EphB2-EphrinB1 interaction kinetics were slightly different, with EphB2 exhibiting a very brief high slope of response at the beginning of the association step that quickly shifted to a slow straight tetramer accumulation phase with no sign of response plateauing. Once placed into dissociation, EphrinB1 immediately lost in the first 40 seconds a portion of bound EphB2 and then the response flatlined. The

immediate high slope of response in the 0-20 sec at the start of the association step and immediate high reverse slope for the first 40 sec of dissociation visualizes a rapid on/off of the EphrinB1-EphB2 dimer.

EphB1-EphrinB2 high-throughput screen

We developed highly sensitive, low volume, chemiluminescent bead-based Alpha proximity assays for use in 384 well plates to measure the protein-protein interactions formed between the EphB1 receptor ectodomain and EphrinB1, EphrinB2, and EphrinB3 ligand ectodomains (Extended Data Fig. 2a), ultimately selecting the EphB1-EphrinB2 interaction to run a high-throughput screen (HTS) (Fig. 1d). Tests of the EphB1-EphrinB2 Alpha assay were conducted before commencing the HTS, including competition experiments with 12-mer peptides EWLS and SNEW that bind within the dimerization pocket formed on the surface of either the EphB1 or EphB2 receptor, respectively, and antagonize their ability to bind EphrinB2[39]. EWLS was observed to reduce the EphB1-EphrinB2 Alpha signal in a concentration-dependent manner with observed half-maximal inhibitory concentration (IC_{50}) of ~4 μM (Extended Data Fig. 2b), similar to the ~10 μM reported for the peptide using a different binding assay[39]. We then tested soluble Reelin protein, which can also bind the EphB1 ectodomain[40], to see if it could interfere with the EphB1-EphrinB2 Alpha assay. This revealed a very strong concentration-dependent reduction in Alpha signal with an IC_{50} of ~50 nM Reelin, and with almost complete inhibition at 200 nM (Extended Data Fig. 2c).

With confidence a robust EphB1-EphrinB2 Alpha assay was developed, we executed a full HTS at the UT Southwestern HTS Core facility and assessed at 5 μM a library of ~240,000 small molecular weight, drug-like chemicals. The average Z' for the HTS was 0.92, indicating a very high-quality screen with little well-to-well or plate-to-plate variability. A total of 1,246 potential hits that reduced the Alpha signal >10% were identified, of which 950 were selected from master plates and retested in the EphB1-EphrinB2 Alpha assay, with positives advancing to additional Alpha assays, ELISA assays, and pulldown assays. This work ultimately resulted in the identification of a single compound (SW056428), for simplicity we call A20, that showed strong ability to reduce both the EphB1-EphrinB2 and EphB2-EphrinB2 interactions, with much less activity towards the EphB4-EphrinB2 interaction (Extended Data Fig. 2d-g).

Lead compound A20 antagonizes the Eph-Ephrin tetramer

BLI was used to probe how A20 might affect Eph-Ephrin binding, focusing first on testing how compound may alter the dynamics of immobilized EphB1 interacting with 100 nM soluble EphrinB2 for a short 80 sec association time (Fig. 1e). In the absence of A20, EphB1 initially bound to EphrinB2 in the first 10 sec with an extremely high 87° slope of response that quickly shifted to a lower slope of 60° for the remainder of the association step. Once placed in the dissociation step, the slope of response abruptly reversed for 20 sec to indicate a very fast-off protein species and then quickly flatlined for the remaining time of dissociation at a level significantly higher than baseline, indicating retention of a very stable complex that did not melt (tetramers). Remarkably, in runs containing A20, there was no effect whatsoever on the initial 10 sec extremely high 87° slope observed at the start of the association step, though there was a clear and very strong concentration-dependent loss of any additional binding as the response was greatly blunted with 10 μM A20 and it flatlined with 100 μM A20. Furthermore, once placed into the dissociation step, the response in runs containing A20 quickly fell to near baseline levels. This indicates A20 has a major effect on Eph-Ephrin binding dynamics, changing them from a 2:1 heterologous/complex-type interaction that produces a highly stable, long-lasting tetramer, to a simple 1:1 dimer-type fast-on/fast-off interaction. The K_D calculated for the EphB1-EphrinB2 interaction using 1:1 binding model in the absence of A20 indicates an extremely high affinity interaction of 0.137 nM (and even higher affinity < 1 pM if calculated using the more appropriate 2:1 heterologous interaction model). However, in the presence of 100 μM A20, the K_D was 46.2 nM, a 337-fold weaker affinity than without the compound, and remarkable similar to the K_{D2} obtained in Fig. 1c for the EphB1-EphrinB2 dimer. It was further noted A20 did not significantly change the rate of association (k_a), which is mainly driven by the formation of the fast-dimer. However, 100 μM A20 did cause a striking 275-fold increase in k_{dis}, reflecting the rapid loss of most all EphrinB2 binding to the immobilized EphB1 and absence of stable tetramers.

To further study dimer-tetramer binding dynamics in the absence of A20, we used shortened association times of 5, 10, 15, 20, 40, and 80 sec and found that >15 sec of association is needed before any tetramers can be detected (Extended Data Fig. 3a). This suggests a critical period of 15-20 sec association is needed to allow for two fast-on/fast-off dimers to form before they can associate into a stable tetramer complex.

We then studied the kinetics of immobilized human EphrinB2 binding to soluble human EphB2 and EphB4 receptor ectodomains, testing the effect of 1, 10, and 100 μM A20 in much longer (800 sec) association times (Fig. 1f). Consistent with the above

data, addition of A20 resulted in reduced tetramer formation during the association step, with a much stronger effect on the EphB2-EphrinB2 interaction compared to the EphB4-EphrinB2 interaction (Extended Data Fig. 3b). Interesting, the inhibitory effect of A20 on either interaction maxed out at the 1 μM concentration, as 10-fold (10 μM) and 100-fold (100 μM) more compound did not provide any enhanced inhibition. This indicates the effective/relative IC_{50} for A20 tetramer inhibition is below 1 μM. It was further noted that similar to EphB1-EphrinB2, the presence of A20 had no effect on the initial very high dimerization slopes observed during the first 20 sec of the EphB2-EphrinB2 association step or the first 100 sec of the EphB4-EphrinB2 association step, consistent with a specific effect of compound on tetramer formation. The minimal effect of A20 on EphB4-EphrinB2 binding combined with the robust 100 sec dimerization slope suggests the interaction between these two proteins is mainly dimer-driven (see more below).

Consistent with the early extreme slope of response representing dimer binding dynamics, the SNEW peptide that binds within the EphB2 dimerization pocket disrupted the EphB2-EphrinB2 dimerization slope (Fig. 1g and Extended Data Fig. 3c). Additional biophysical studies showed A20 acts as a reversible competitive antagonist of EphB-EphrinB tetramer binding (Extended Data Fig. 3d-f), and that A20 can melt pre-existing tetramers (Extended Data Fig. 3g). Mass photometry further confirmed that EphB2 and EphrinB2 form tetramers in solution that can be disrupted by A20 (Fig. 1h). We also found A20 can reduce tetramer formation between EphB1 and EphB2 receptors binding to EphrinB1 and EphrinB3 (Extended Data Fig. 3h), and even tetramers formed between A-class molecules (EphA3-EphrinA1 and EphA3-EphrinA5) and cross-class A/B interaction molecules (EphB2-EphrinA5) (Extended Data Fig. 3i-j). Altogether, our data indicates A20 selectively targets tetramers formed by most if not all Eph-Ephrin family members, and is consistent with a general conservation of the tetramer interface structures of this large family of promiscuously-interacting receptors and ligands.

Tetramer inhibitors can be improved

In addition to A20 that was identified in the 240,000 EphB1-EphrinB2 Alpha screen (Extended Data Fig. 2f), we realized that 66 of the top 1,246 primary hit compounds identified in the HTS were related to A20 in that they all contained an 8-hydroxyquinoline (8-HQ) ring structure (Supplementary Table 1). In our own medicinal chemistry campaign, we generated an additional 25 novel 8-HQ chemicals (Fig. 1i,

Extended Data Fig. 4a-g, Supplementary Table 2). We used two methods to characterize tetramer inhibitor activities using BLI. The first involved sensorgram area under the curve (AUC) analysis to calculate the percentage of the protein-protein interaction of interest that is lost by addition of 3.2 μM of a selected compound during an 80 sec association time. At this concentration a potent compound will inhibit the majority of tetramers (surmountable), though a very low level of insurmountable tetramers can still form and accumulate in the presence of compound, especially in BLI runs with extended association times. In an example of this analysis, novel compound A20-I shows the typical strong tetramer inhibitor activity with greatest ability to reduce the EphB2-EphrinB2 interaction (61.8% of the association interaction was inhibited), followed by the EphB1-EphrinB2 interaction (36.6% inhibited), and with weakest activity towards the dimer-driven EphB4-EphrinB2 interaction (13.9% inhibited) (Extended Data Fig. 4h).

The second method determines the inhibitor concentration that reduces the protein-protein interaction 50% (IC_{50}) and the inhibition constant (K_i), which gives an estimate of how strongly a competitive inhibitor may bind to its target protein. These calculations utilize AUC information, though here a concentration-response series of sensorgrams for a compound of interest, typically 0.0, 0.1, 0.2, 0.4, 0.8, 1.6, and 3.2 μM, are obtained. The AUC of each biosensor response is then used to determine both an absolute IC_{50} and a relative IC_{50}. The relative IC_{50} is determined by first subtracting the AUC of the max control sensorgram runs from the AUCs of the concentration-response runs of the compound under analysis, this eliminates the contribution of dimer binding and insurmountable tetramer binding (Extended Data Fig. 3b) from the IC_{50} calculation and provides for a more accurate determination of a compound's intrinsic tetramer inhibitor activity. Examples of concentration-response BLI runs and AUC comparisons of novel compounds are provided (Extended Data Fig. 4i-j), as are the details of a new computer program, Find50.py, we developed to help collect and compare AUCs to calculate IC_{50} and K_i values (Extended Data Fig. 4k), which are presented in Supplementary Tables 1 and 2. A particularly potent novel compound we synthesized, BQPB4, shows very strong ability to block the tetramer with improved IC_{50} and K_i values compared to A20 (Fig. 1j). It was further noted that BQPB4 can also target the small amount of insurmountable tetramers that typically form in the presence of other A20 compounds.

Tetramer inhibitor pharmacology

Salts of interesting compounds were subjected to a number of *in vitro* pharmacokinetic (PK) studies at the UT Southwestern Preclinicial Core facility to assess solubility, plasma stability, and metabolic stability, finding they were generally soluble and stable, noting that potent inhibitor BQPB4 exhibited superior stability profiles (Extended Data Fig. 5a-b). A20 was evaluated for its absorption, distribution, metabolism, excretion, and toxicity (ADMET) following a single intravenous (i.v.) injection, intraperitoneal (i.p.) injection, or oral (p.o.) dose, finding that compound in all three administration methods quickly distributed to the plasma, liver, and skin, and passed the blood brain barrier (BBB) to reach the brain and spinal cord (Extended Data Fig. 5c-e). Similar studies of novel compounds A20-I (p.o. dosed) and QPB4-Bn (i.p. dosed) also indicated favorable ADMET properties, indicating compounds are orally available and maintained concentrations close to their tetramer inhibitor IC_{50} values up to 24 hr post dosing (Extended Data Fig. 5f-g). Multiple consecutive dosing of mice with A20 and novel compounds A20-I, 3511-I, and BQPB4 further indicated tetramer inhibitors were all well tolerated with no obvious negative effects to the animal (Extended Data Fig. 5g).

Tetramer inhibitors target forward signaling

We next sought to investigate the effect of tetramer inhibitors on Eph-Ephrin bidirectional signaling. Focusing on forward signaling mediated by the EphB intracellular tyrosine kinase catalytic domain, we first developed rigorous methods to accurately detect and quantitatively measure a receptor's activation state. To do this, various commercially available antibodies advertised to be raised against EphB1 or EphB2 were first tested by adding them to total cell protein lysates prepared from wild-type (WT) animals to immunoprecipitate (IP) the receptor protein, which was then visualized by adding ATP in a classic *in vitro* tyrosine kinase autophosphorylation assay[4,41]. We took advantage of our extensive collection of gene-targeted *EphB1* and *EphB2* mutant mice to obtain control lysates[4,42-45]. While no antibodies worked to detect EphB1, we were successful with the EphB2 reagents and determined that high levels of catalytically active receptor could be precipitated from lysates prepared from mid-gestation mouse embryos (Fig. 2a) and from adult brains (Extended Data Fig. 6a). Most importantly, following addition of ATP, the EphB2 protein IPed from lysates of WT and F620D point mutant (which expresses a dysregulated overactive kinase) animals showed a very intense phosphotyrosine signal that was detected with multiple anti-phosphotyrosine antibodies, including an anti-phospho-EphB specific antibody that specifically recognizes a conserved tyrosine residue present in the juxtamembrane

segment of EphB1 and EphB2 (pYIPD), as well as the general anti-phosphotyrosine antibodies pTyr1000 and 4G10 Platinum. It was further noted that activated, tyrosine phosphorylated pEphB2 protein exhibited a slightly retarded migration in reducing SDS-PAGE gels and presented as a protein band just above the 130 kDa protein standard that is distinct from the unphosphorylated, total tEphB2 species, which migrated just below the 130 kDa marker. Key mutant control lysates prove the signals detected were indeed EphB2 protein. As such, the knockout (KO) animals showed no EphB2 protein, the lacZ intracellular truncated mutant expressed a much larger ~250 kDa EphB2-βgal fusion protein that retains its intracellular juxtamembrane segment and properly localizes to the membrane, but lacks the tyrosine kinase catalytic domain and thus shows no phosphorylation after addition of ATP, and the K661R kinase-dead point mutation that produces a full-length EphB2 protein also did not become phosphorylated after addition of ATP. These data gave us confidence that the various reagents employed below genuinely detect EphB2 protein, both the inactive/ unphosphorylated total tEphB2 as well as the active/phosphorylated pEphB2 species.

We next developed methods to precisely measure how much EphB2 protein in any one lysate is in the active, tyrosine phosphorylated pEphB2 state. To accomplish this, we used Cos1 cells that endogenously express EphB2 to determine how well stimulation with 1.5 ug/ml (30 nM) soluble EphrinB2-Fc could activate the receptor, testing both unclustered and pre-clustered forms of the ectodomain. Here, following a time course of stimulation with EphrinB2-Fc, cell lysates were mixed with pTyr1000-conjugated beads and then 100% of the precipitated phosphotyrosine-containing proteins were run on an SDS-PAGE gel next to a lane loaded with 1% of the whole cell lysate taken prior to IP. After immunoblotting for EphB2, band signals corresponding to pEphB2 (pTyr1000 IP lane) and tEphB2 (lysate lane) were determined and used in a simple equation to calculate the percentage of EphB2 in a lysate that is in the tyrosine phosphorylated pEphB2 state (% pEphB2) (Fig. 2b and Extended Data Fig. 6b). The data showed that while very low levels of % pEphB2 were detected in unstimulated cells (<0.1%), cells stimulated with EphrinB2-Fc showed a gradual, time-dependent increase in % pEphB2 reaching 0.72% for the unclustered reagent and 2.27% for the pre-clustered reagent at 32 min, which was 8-fold and 45-fold higher than the unstimulated cells, respectively. Cos1 cells were then stimulated with pre-clustered EphrinB2-Fc for 32 min and incubated with increasing amounts of a combination of three tetracyclines we previously reported act as a pan EphB tyrosine kinase inhibitor (Minocycline/Chlortetracycline/Demeclocycline, MCD)[37]. This led to a concentration-dependent decrease in the pEphB2 band intensity in the immunoblot and, when the %

pEphB2 was calculated using the pEphB2 and tEphB2 signals, resulted in an IC_{50} of 121.4 μM (Fig. 2c and Extended Data Fig. 6c). Cos1 cells growing at lower density were then used to test novel compounds A20-I and BQPB4, and compare to MCD. We found more sparsely plated cells responded much better to EphrinB2-Fc stimulations such that 5-6% pEphB2 in a cell could be achieved after 32 min of stimulation with the unclustered ectodomain. Addition of increasing MCD again resulted in a concentration-dependent decrease in pEphB2 levels and calculated % pEphB2, here with another relatively poor IC_{50} of 71.2 μM, while addition of A20-I was able to reduce pEphB2 levels and % pEphB2 at much lower concentrations with an IC_{50} of 8.5 μM, and BQPB4 performed even better with an IC_{50} of 3.2 μM (Fig. 2d and Extended Data Fig. 6d). In this direct comparison, it is clear that A20-I and BQPB4 with >8-fold and >22-fold more potent ability to reduce % pEphB2 compared to MCD, respectively, are more powerful inhibitors of EphB2 forward signaling.

We next studied whether A20 would affect the ability of EphrinB2-Fc to bind, cluster, and activate EphB2 on the cell surface. Here, Cos1 cells plated on cover slips were stimulated with pre-clustered EphrinB2-Fc for 30 min without or with 40 μM A20 and then fixed and subjected to immunofluorescence staining to identify large spots of clustered EphrinB2-bound EphB2 and if the spots contained detectable levels of phosphotyrosine (Extended Data Fig. 6e). Quantification of the data revealed A20 significantly reduced the number of spots and fewer of the spots were phosphotyrosine positive. This data indicates A20 can reduce the ability of EphrinB2 to bind and cluster EphB2, thereby inhibiting activation of the receptor's intracellular tyrosine kinase catalytic domain.

We next developed methods to assess pEphB2 *in vivo* in order to examine the effect of tetramer inhibitors once administered to a living animal. We employed protocols similar to above, this time using anti-phospho-EphB, pTyr1000, or 4G10 Platinum antibodies to IP pEphB2 protein from lysates of *EphB2* WT and KO mouse embryos collected at E14.5. This revealed a fairly low % pEphB2 at mid-gestation of 0.73%, 0.60%, 0.82%, respectively, and 1.00% if all three antibodies were combined in the IP (Fig. 2e and Extended Data Fig. 6f). We then attempted to IP and identify pEphB2 in the adult mouse brain where the receptor also shows very high expression, but failed to detect any activated protein, even in the F620D dysregulated kinase mouse (Fig. 2f). Realizing the level of pEphB2 that can be detected *in vivo* might be under extreme tight control, we next made brain lysates at different developmental stages and found the E16.5 embryonic brain contained 1.39% active pEphB2 and this

gradually decreased through postnatal stages to become a very low, almost undetectable 0.09% by 84 days (Fig. 2g and Extended Data Fig. 6g).

The low, barely detectable amounts of % pEphB2 present in adult tissues made it difficult to assess the effect of tetramer inhibitors *in vivo* after dosing them into animals. We therefore turned to postnatal stages and found sufficient % pEphB2 could be detected in the intestines of vehicle dosed pups collected at P8, and that this was significantly reduced in animals i.p. injected with A20 (Fig. 2h and Extended Data Fig. 6h). These experiments also revealed another potent Eph-Ephrin tetramer inhibitor, ethylenediaminetetraacetic acid (EDTA, tetrasodium salt), led to reduced % pEphB2. As described in the accompanying manuscript[46], we identified EDTA as a tetramer inhibitor in our ongoing efforts to better understand the molecular mechanisms that govern tetramer assembly[46]. A20 and EDTA were further tested in additional, similarly prepared kidney and intestine lysates, this time using either pTyr1000-conjugated beads or SH2 superbinder-conjugated beads for the IPs. Here, we found both A20 and EDTA resulted in significant reductions in % pEphB2 as well as highly significant reductions in pEphB2 levels (Fig. 2i,j and Extended Data Fig. 6i and j). Altogether, the above data shows activation of EphB2 is reduced in animals dosed with a tetramer inhibitor.

Tetramer inhibitors target reverse signaling

We next turned our attention to reverse signaling and again needed to validate antibody reagents and develop methods to quantitatively measure active, tyrosine phosphorylated pEphrinB2 protein. Adopting our strategy for analysis of forward signaling, we first assessed mid-gestation mouse embryo protein lysates expecting they would contain elevated amounts of pEphrinB2. As crucial controls for these experiments, we employed our two previously described gene-targeted *EphrinB2* (*Efnb2*) mutations, termed lacZ and 6YFdV[47,48]. *EphrinB2* lacZ expresses a properly localized membrane-anchored truncated EphrinB2-βgal fusion protein lacking its intracellular tail, and 6YFdV is a multiple point mutant in which the six intracellular tyrosine residues are changed to phenylalanine to prevent phosphorylation and coupling to SH2 domain proteins and with the C-terminal valine residue important for coupling to intracellular PDZ domain containing proteins also deleted. Phosphotyrosine proteins were first IPed from *EphrinB2* +/+ WT and 6YFdV/6YFdV homozygous mutant embryo lysates using either pTyr1000-conjugated beads or 4G10 Platinum antibodies bound to Protein G sepharose, and then immunoblotted with goat anti-EphrinB2

antibodies (Fig. 3a and Extended Data Fig. 7a). This revealed a small, though detectable amount of pEphrinB2 protein, especially using the pTyr1000 beads, that was present in the WT lysate but not in the 6YFdV lysate. Quantification of the pTyr1000 bead IP indicated 0.435% of the EphrinB2 protein was in the active tyrosine phosphorylated pEphrinB2 state in mid-gestation embryos. SH2 superbinder beads could also IP activated pEphrinB2 protein from embryo lysates (Fig. 3b and Extended Data Fig. 7b). In this experiment, pEphrinB2 represented 0.14% of the total EphrinB2 protein, and was comparable to the 0.13% determined from the pTyr1000 bead IP.

Having developed methods to detect activated pEphrinB2, we then stimulated cultured pancreatic stellate cells which endogenously express the ligand protein with 2.5 ug/ml (30 nM) unclustered EphB2-Fc ectodomain. The data showed BQPB4 effectively reduced the ability of EphB2-Fc to stimulate EphrinB2 reverse signaling in a concentration-dependent fashion as measured by a reduction in % pEphrinB2 (IC_{50} = 1.5 μM) and an overall reduction in pEphrinB2 levels (IC_{50} = 1.5 μM) (Fig. 3c and Extended Data Fig. 7c). EDTA exhibited a similar concentration-dependent ability to reduce the % pEphrinB2 (IC_{50} = 1.1 μM) and pEphrinB2 levels (IC_{50} = 1.9 μM) (Fig. 3d and Extended Data Fig. 7d). We then assessed ability of tetramer inhibitor to reduce the activation and phosphorylation of EphrinB2 *in vivo* using lysates from P8 intestines collected from a group of animals dosed with EDTA. The data showed compound significantly reduced % pEphrinB2 and pEphrinB2 levels without affecting total tEphrinB2 protein levels (Fig. 3e and Extended Data Fig. 7e). Altogether, the above data shows we can detect reduced activation of EphrinB2 reverse signaling in animals dosed with a tetramer inhibitor.

Tetramer inhibitors blunt inflammatory pain

Having demonstrated tetramer inhibitors pass the BBB and exhibit on-target abilities to reduce both EphB forward and EphrinB reverse signaling, we next investigated how well A20 compounds may counter chronic pain. Inflammatory pain induced by intraplantar injection of complete freund's adjuvant (CFA) into the mouse left hind paw provides a robust model that results in ~2 weeks of localized, painful paw swelling that can be assess on multiple days for heat (thermal) and touch (mechanical) sensitivity (Fig. 4a). For each day of data collection, the average uninjured right hind paw response was divided by the average injured left hind paw response to obtain a pain ratio which was then plotted and subjected to appropriate statistical analysis. In all of the behavior studies, the person conducting the pain testing (K.C.) was completely

blinded to genotypes and/or treatment groups as the person who grew, handled, and administered compounds to mice was a different person (M.H.).

We first revisited CFA pain responses in *EphB1* -/- knockout (KO) mice[28,42] and examined *EphB1* lacZ/lacZ (LZ) mutant mice[45] that have not previously been studied for pain. As the *EphB1* LZ mice express an intracellular truncated EphB1-βgal fusion protein that lacks its intracellular tyrosine kinase domain, SAM domain, and C-terminal tail that normally couples the receptor to PDZ domain proteins, it is unable to transduce classic forward signals. The EphB1-βgal fusion protein does, however, retain its extracellular, transmembrane, and juxtamembrane segments so it is still membrane localized and able to bind to EphrinB proteins to activate reverse signaling in a similar fashion we originally described for the EphB2-βgal fusion protein[4]. As expected, WT mice exhibited long-lasting significantly increased thermal pain in their CFA-injured hind paw over multiple days (Fig. 4b and Extended Data Fig. 8a). The *EphB1* KO mice showed no increased thermal pain over baseline, also as expected, and is consistent with previous work that demonstrated deletion of this receptor leads to mice refractory to chronic pain [23,25,27,28]. Curiously, the *EphB1* LZ mice did not behave like the knockouts, instead they showed a transient and highly significant increase in thermal pain like the WT mice, but then within a couple days began to look more like the KO mice and showed low levels of thermal pain. Statistical analysis showed that at day +1 post-CFA injury, both the WT and LZ mice exhibited strong increases in their pain ratios that were significantly different from the KO mice who remained pain free. However, by days +6 and +9, only the WT mice exhibited significant pain, the LZ mice now mimicked the KO mice and appeared relatively pain free. Similar results were obtained in tests for mechanical pain, with both the WT and LZ mice showing significant increased touch pain sensitivity early at +3 days post-CFA, though by day +8 only the WT mice continued to experience elevated pain (Fig. 4c and Extended Data Fig. 8a). As the LZ mice exhibit increased pain early after CFA injury and since the intracellular truncated EphB1-βgal fusion protein cannot transduce forward signals but can still act as a ligand to bind Ephrins and activate reverse signaling, the data suggests reverse signaling may be more important for early stages of chronic pain, while EphB1 forward signaling becomes more important for later stages (see below).

We next tested for thermal pain a group of WT mice that were i.p. injected with A20, MCD, or a combination of A20+MCD, finding animals that received 20 mg/kg doses of the tetramer inhibitor exhibited significantly reduced thermal pain at +3 days post-CFA compared to the vehicle treated mice, though MCD kinase inhibitor had no significant effect on pain (Fig. 4d). Other groups of mice i.p. injected with 20 mg/kg of

tetramer inhibitors A20 and QPB4-Bn (Fig. 4e), or QPB4 and QPP127 all showed significant reductions in pain compared to the vehicle controls (Fig. 4f) (Extended Data Fig. 8b). Given this promising early work, we then advanced to a long term CFA study where A20 was either i.p. injected or p.o. oral dosed at 20 mg/kg and mice tested for thermal pain (Fig. 4g and Extended Data Fig. 8c) and mechanical pain (Fig. 4h and Extended Data Fig. 8d) for a two week period. The data showed A20, whether injected or orally dosed strongly blunted the elevated heat and touch pain sensitivity caused by CFA.

We then employed another inflammatory agent, Zymosan, to induced an intense short-lasting increase in thermal and mechanical pain, first testing a group of WT and *EphB1* KO mice (Fig. 4i and Extended Data Fig. 8e), revealing that loss of EphB1 receptor expression in the KO significantly blunted both the elevated heat and touch pain responses compared to the WT control mice. We also examined a group of EphrinB2 reverse signaling mutant mice (*EphrinB2* lacZ/6YFdV), which are viable, normal appearing long-lived animals, and found that they too were highly refractory to developing enhance injury-induced pain (Fig. 4j and Extended Data Fig. 8f). This data indicates reverse signaling mediated by an intact EphrinB2 intracellular domain is key for the development of inflammatory pain.

Oral dosing of novel A20 tetramer inhibitors 3511-I and BQPB4 at 20 mg/kg was then tested in the Zymosan model and found to significantly blunt pain (Fig. 4k and Extended Data Fig. 8g). Oral dose response studies testing 5, 10, and 20 mg/kg further revealed that A20 (Extended Data Fig. 8h) and to a greater extent BQPB4 (Fig. 4l and Extended Data Fig. 8i) led to significantly diminished pain, even at the lowest dose tested.

Tetramer inhibitors reduce dorsal horn neuron activation

Chronic pain generating nerve injuries/insults overstimulate nociceptor C-fibers whose central projections form synapses with DH neurons in the superficial spinal cord. The excessive firing of C-fibers increases synaptic activity and post-synaptic activation of the NMDAR, leading to calcium influx and downstream signaling that activates DH neurons and triggers plasticity (LTP), which results in central sensitization. Consistent with the post-synaptic localization of EphB1[36], its key role in pain, and its ability to both physically associate with the NMDAR NR1 subunit and induce tyrosine phosphorylation of the NR2 subunit[29,30], KO mice exhibit significantly reduced numbers of c-Fos expressing DH neurons after an inflammatory insult[28], and stimulation of C-fibers in

living *EphB1* KO mice failed to induce LTP[25]. To better visualize DH neuron activation, we utilized a genetic tool, *Trap2*, that expresses CreERT2 only in activated neurons and when combined with a *Rosa26-stop-tdTomato* Cre indicator (*Ai9*) and an i.p. injection of 4-hydroxytamoxifen (4-OHT), will permanently label with red fluorescence only neurons that were activated for a short window of time (~8 hr) until the 4-OHT is degraded[49,50]. We first crossed mice that carried *Trap2* and *Ai9* elements with mice that contained the *EphB1* KO mutation to generate *EphB1*+/+, +/-, and -/- animals that contained *Trap2* and *Ai9*. The left hind paws were injected with CFA to provide an inflammatory insult, and then after 4 hr to allow DH neuron activation, the mice were injected i.p. with 4-OHT to induce permanent strong expression of the tdTomato red fluorescent protein. Two weeks later, animals were perfusion fixed, lumbar spinal cords vibratome sectioned, and viewed with a fluorescent microscope to reveal the red labeled neurons that were activated ~4-12 hr post-CFA. Quantification determined approximately 3 times more red labeled neurons on the injured side versus the uninjured side in the WT mice, whereas +/- and -/- spinal cords showed significantly reduced ratios, with the KO exhibiting a near equal number of neurons on both sides, indicating little, if any, activation of DH neurons in the mutant (Fig. 5a). We then tested if injection of A20 or MCD would affect neuronal activity in the dorsal horn, determining that tetramer inhibitor, but not kinase inhibitor, significantly reduced DH neuron activation following CFA insult (Fig. 5b). Additional studies determined that 3511-I and BQPB4 also reduced DH neuron activation in the lumbar spinal cord (Extended Data Fig. 9).

Tetramer inhibitors blunt opioid withdrawal

Remarkably, like in chronic pain, it has been reported that expression of EphB1 is upregulated in the dorsal horn of the spinal cord in mice given escalating doses of morphine[51], and that *EphB1* -/- KO mice exhibit greatly reduced withdrawal behaviors[23]. A role for EphB1 in mediating opioid dependence is consistent with its ability to control the post-synaptic localization and activation of the NMDAR[29,30,36], which is also implicated in mediating the adverse effects of opioid withdrawal[52]. We first confirmed the role of EphB1 in withdrawal behaviors by subjecting a group of *EphB1* KO and WT littermate mice to IP injections of increasing morphine every 12 hr for 5 days. Withdrawal was then precipitated with a subcutaneous injection of naloxone hydrochloride, and animals monitored for 30 min for adverse behaviors by the examiner (by S. Birnbaum, Director of the Rodent Behavior Core) who was blinded to

animal genotypes or compound dosing regimen (by M.H.). Major adverse withdrawal events monitored in mice include an unusual and easily scored jumping behavior, as well as presence of diarrhea, tremor, wet dog shakes, and ptosis. Plotting the total number of jumps each mouse made showed that the WT mice exhibited significantly more jumps compared to the KO mice (Fig. 6a). We then assessed if i.p. injection of A20 would affect withdrawal behaviors, in one experiment using CD1 strain mice and in another C57BL/6 mice. Combined, the A20 treated animals exhibited a highly significant reduction in jumps compared to vehicle (Fig. 6b). The C57BL/6 mice were additionally scored at 5 min intervals for diarrhea, tremor, and ptosis. The tetramer inhibitor treated mice showed reduced incidence of each parameter (Fig. 6c).

Discussion

We present our identification and characterization of small molecules that disrupt the Eph-Ephrin tetramer, which provide a novel method to counter the many chronic diseases associated with excessive expression and pathological signaling by this large family of interacting proteins (Fig. 6d). Our drug discovery efforts were directed toward the interaction of EphB1 with one of its ligands, EphrinB2, mediated by extracellular segments of these two proteins. The focus was on finding a way to effectively target the receptor-ligand interaction as we predicted such an approach would interfere with both EphB forward signaling and EphrinB reverse signaling. This is in contrast to the more traditional search for a tyrosine kinase inhibitor (like MCD) that would only target the catalytic function of the Eph molecule. Indeed, work presented here and that presented on pancreatic cancer in the accompanying manuscript by our London collaborators[53] show reverse signaling is involved in chronic pain and cancer cell migration, and that A20 tetramer inhibitors are effective in countering both. With regards to the apparent early role for nociceptor-expressed pre-synaptic EphrinB2 reverse signaling in chronic pain, we liken it may be quite similar to the previously described pre-synaptic retrograde signaling activities for EphrinB proteins in the induction of LTP of hippocampal mossy fiber–CA3 synapses[54]. Other attempts to target Eph-Ephrin receptor-ligand interactions have focused on the dimerization interface, like the SNEW and EWLS peptides[39] incorporated in our studies, as well as a number of small molecules[55-61]. However, none of these dimerization inhibitors appear to have activities that come close to what we describe here for tetramerization inhibitors as we show A20 compounds have submicromolar $IC_{50's}$ and low nanomolar $K_{i's}$, they can block both Eph forward and Ephrin reverse cell signaling, and exhibit potent drug-like

qualities to blunt chronic pain and opioid withdrawal *in vivo*. We believe our approach is more comprehensive, starting with a HTS screen of almost 240,000 compounds that identified 67 different A20 type 8-HQ chemicals out of the top 1,246 hits (Supplementary Table 1), and an extensive medicinal chemistry campaign that resulted in improved tetramer inhibitors with even more potent activities, like BQPB4 (Supplementary Table 2).

While the binding kinetics we described above using BLI for all the various EphB-EphrinB macromolecular interactions are complicated and show clear differences, they all are extremely high affinity interactions with K_D values in the low nanomolar to picomolar range. One of the most striking features we have uncovered is that only some Eph-Ephrin interactions are tetramer-driven and strongly disrupted by tetramer inhibitors, like EphB1-EphrinB2 and EphB2-EphrinB2, whereas other interactions are more dimer-driven and only slightly disrupted by the tetramer inhibitors, like EphB4-EphrinB2. Indeed, while co-crystal of EphB2-EphrinB2 showed these two proteins assemble into a circular tetramer[3], co-crystals and other biophysical studies reported for EphB4-EphrinB2 do not indicate a tetramer is formed[62,63]. We believe this is a very important feature of tetramer inhibitors as they are further developed. EphB4 is the only essential EphB receptor, knockout mice are embryonic lethal and show severe cardiovascular malformations[64,65], and other studies indicate its continued importance in the adult[66,67]. It is also noteworthy to discuss that EphrinB2 is also a key player in cardiovascular development and blood vessel remodeling and angiogenesis, with EphrinB2 expressed on arterial cells and EphB4 on venous cells[64,68]. Thus, EphB4-EphrinB2 cell-cell contact in endothelial cells is essential to help regulate blood vessel remodeling and integrity, and may be an interaction that needs to be preserved. As tetramer inhibitors exhibit only mild effects on the EphB4-EphrinB2 interaction, we anticipate they may exhibit robust ability to counter pathological expression and signaling of the EphB1 and EphB2 tetramer-driven receptors, while leaving intact the EphB4 interactions and minimizing any unwanted effects on the vascular system. Indeed, we have not noticed any negative effects of compound administration into animals and they did not exhibit any signs of issues with the endothelium. We are fascinated by the fact that the same EphrinB2 ligand can apparently form tetramers with some receptors, like EphB1 and EphB2, but only dimers with other receptors like EphB4. We also uncovered another example of a similar tetramer/dimer difference with the A-class Eph/Ephrin molecules, finding that EphA3 interacts mainly as a dimer with EphrinA5 and as a tetramer with EphrinA1 (Extended Data Fig. 3j).

Our study also uncovered another important concept regarding dimer-tetramer dynamics and whether the binding affinity behind assembly of the Eph-Ephrin macromolecular complexes is due to dimer interactions or tetramer interactions. While the evidence is not all that strong, the literature basically states that Eph-Ephrin dimer binding is the high-affinity interaction that drives assembly. Our studies indicate this notion needs to be reconsidered. The BLI experiment shown in Fig. 1e looking at EphB1-EphrinB2 binding particularly brings this to light as it demonstrates that A20 effectively disrupts all tetramer formation at 100 μM without any effect on dimer binding kinetics. As such, with 100 μM A20 we can isolate dimer formation, and in doing so find it exhibits simple 1:1 binding kinetics with very fast-on/fast-off dynamics. The K_D calculated in this experiment in the presence of A20 was 46.2 nM and reflects simple dimer binding kinetics, whereas the K_D for the full interaction when A20 is omitted, reflects both dimer and tetramer binding, calculated to be 0.137 nM. Clearly, these results indicate that dimer binding contributes marginally to the overall binding affinity of the interaction, and that it is tetramer formation that is the driving force behind the strength of the macromolecular assembly. What drives dimer versus tetramer formation and how do tetramer inhibitors act to disrupt the tetramer is the focus of our accompanying manuscript[46].

Another important consideration for future development of tetramer inhibitors is their target specificity and whether it would be better to have a small molecule with exquisite specificity for a single molecular interaction or one with broad ability to hit multiple targets. Regarding chronic pain, while our work mainly focuses on EphB1/EphB2, there are reports that indicate other Eph receptors may be involved, including EphB3[69] and EphA4, EphA7, EphA8[20]. An effective anti-Eph/Ephrin therapeutic to counter excessive signaling in chronic pain might need to target not just the tetramers formed by EphB1 and EphB2, but tetramers formed by these other Eph receptors. Likewise, in addition to EphB2, the EphA2 and EphA3 receptors interacting with EphrinA1 may also contribute to chronic fibrotic pathologies[70,71]. We show our tetramerization inhibitors effectively disrupt tetramers formed by both B- and A- class molecules, as well as cross-class A/B tetramers (e.g. EphB2-EphrinA5 tetramers). Thus, we have reason to believe an innovative therapeutic might be a small molecule with broad capabilities to target both A- and B- class tetramers. This may be particularly important considering that many people suffer from multiple comorbid chronic conditions and may show overexpression of many of the 14 different Eph receptors in different diseased organs. In contrast, if tetramer inhibitors with greater selectively are warranted, our ongoing medicinal chemistry structure activity

relationship campaign indicate compounds that exhibit more specific abilities to disrupt either EphB1 or EphB2 tetramers are possible and could be further explored.

Methods

Biolayer Interferometry

Eph-Ephrin binding kinetics were analyzed using BLI and an Octet RED384 system (ForteBio/Sartorius) and various commercially available recombinant Eph and Ephrin ectodomain proteins that contained C-terminal Fc and/or His tagged epitopes (sources indicated below). Unconjugated human Fc only protein was also utilize in BLI as negative control and showed no binding in the experiments. Reconstituted ectodomain proteins were routinely passed through Zeba desalting columns before use (Thermo Scientific, 89890). The buffer conditions used were PBS pH 7.4 containing 0.02% Tween 20 (PBST). In most experiments, Fc-tagged Eph or Ephrin ectodomains were first sparsely loaded onto Octet Anti-Human IgG Fc Capture (AHC and AHC2) Biosensor Chips (Sartorius, 18-5143) using 0.625-0.125 ug/ml of the Fc protein, and then after washing and obtaining baseline measurements, the biosensors were placed into wells that contained the desired concentration of soluble interacting partner for the association step for the desired period of time, after which the biosensors were returned to the baseline well for dissociation step. In some experiments ectodomain proteins were sparsely biotinylated using EZ-Link NHS-PEG4-Biotin (Thermo Scientific, A39259) and then passed through Zeba desalting columns before loading onto Octet Super Streptavidin (SSA) Biosensor Chips (Sartorius, 18-5057) and subjecting to baseline, association, and dissociation steps. In experiments that assessed a tetramer inhibitor compound, the baseline and association wells also contained the diluted compound in 1% DMSO final as compounds were dissolved and diluted to 100X final concentrations in DMSO prior to being diluted 1:100 in PBST. Data acquisition is performed using the Octet RED384 instrument and its associated customizable software to automate the process and generate output files using Octet Analysis Studio Software to visualize the sensorgram data and calculate the kinetic parameters of the molecular interaction under study.

Alpha assays and HTS

Recombinant rat EphB1-Fc, mouse EphB2-Fc-His, human EphB4-Fc ectodomain proteins, and human Fc only protein as negative control and various EphrinB-His ectodomain proteins were combined with Alpha Protein A Donor Beads (PerkinElmer/Revvity, AS102D) and Alpha Anti-6xHis Acceptor Beads (PerkinElmer/Revvity, AL178C) in 1x AlphaLISA Hiblock Buffer (PerkinElmer/Revvity, AL004C)(25 mM HEPES, pH 7.4,

0.1% Casein, 1 mg/mL Dextran-500, 0.5% Triton X-100, 0.5% Blocking reagent, 0.5%BSA and 0.05% Proclin-300) in 384 well untreated AlphaPlates (PerkinElmer/ Revvity, 6057350). The EphB-Fc ectodomain decorated Protein A donor beads and EphrinB-His ectodomain decorated anti-6His acceptor beads were allowed to bind each other and reach equilibrium (>3 hr), after which plates were placed into an EnVision Multilabel Plate Reader (PerkinElmer) to generate singlet oxygen molecules by high energy irradiation of the donor beads which will travel over a constrained distance to excite the acceptor beads and produce a chemiluminescent signal. The basic idea is that Eph-Ephrin binding will bring donor and acceptor beads into close proximity to transfer energy and give a strong signal, whereas a compound from the HTS library that interferes with Eph-Ephrin binding would lead to diminished chemiluminescence. The 240,000 compound chemical library file that was screened in the UT Southwestern HTS Core facility was composed of compounds obtained from various suppliers, including ChemBridge, Chemical Diversity, ComGenex, TimTek, Prestwick, and the NIH phase 1 collection. The chemical library is stored as five identical master sets ([compound] ~10 mM) in uniquely barcoded, 384-well microtiter plates. Three cherry-picking plate sets (384-well plates, [compound] ~5 mM) are derived from one master plate set. Five to six screening masters (384-well plates, [compound]~0.5 mM) are prepared from one of the cherry-picking plate sets. Each screening master set supplies 30 to 50 high throughput screens. All of the plates sets derived from a master plate set are barcoded and tracked using an inventory management system. Copies of the chemical library are stored frozen in DMSO in plates at -80 or -20 °C. The quality of compounds in the library is monitored by tracking the hit rates in experiments and freeze thaw cycles are counted. Copies of the library are archived usually due to deterioration of the plates as a result of repeated resealing rather than any decrease in biological activity of the compounds. Small amounts of lead hits were cherry-picked from master plates and used for confirmation Alpha, ELISA, and pull-down assays. Commericial sources were used for resupply of interesting compounds and to obtain additional available analogs.

ELISA assays

Recombinant rat EphB1-Fc, mouse EphB2-Fc-His, human EphB4-Fc ectodomain proteins, and human Fc only protein as negative control were added for 1 hr to 96 well Pierce Protein A Coated Plates (Thermo Scientific, 15154) that had been pre-blocked in 1x AlphaLISA Hiblock Buffer. Wells were then washed in PBST and incubated for 1 hr

with soluble mouse EphrinB2-His ectodomain protein in 1x AlphaLISA Hiblock Buffer in the absence or presence of selected concentration of compound diluted in DMSO (1% DMSO final), washed again, reacted with HRP-conjugated 6xHis Tag (C-term) Monoclonal Antibody (3D5) (Thermo Scientific, R931-25), and then visualized using ELISA Pico Chemiluminescent Substrate (Thermo Scientific, 37069) and a luminometer.

Pull-down assays

Recombinant rat EphB1-Fc, mouse EphB2-Fc-His, human EphB4-Fc ectodomain proteins, and human Fc only protein as negative control were mixed for 1 hr with Protein G Sepharose beads (Thermo Scientific, 101242) that had been pre-blocked in 1x HiBlock Buffer. Beads were then washed and incubated for 1 hr with soluble mouse EphrinB2-His ectodomain protein in 1x AlphaLISA Hiblock Buffer in the absence or presence of selected concentration of compound diluted in DMSO (1% DMSO final), washed again, and then proteins eluted from the beads in 6X SDS sample buffer, resolved on SDS-PAGE gels, transferred to membrane, and immunoblotted with anti-His or anti-Fc antibodies.

Chemical synthesis

Detailed information concerning chemical synthesis is provided in the Supplementary Chemistry Information.

Cell stimulations and protein lysates

Cos1 cells were grown in 6 well culture plates in DMEM medium containing 10% fetal bovine serum, 2 mM L-Glutamine and antibiotics (1% penicillin and streptomycin). Pancreatic Stellate cells were grown in 6 well culture plates in DMEM/F12 medium containing 10% fetal bovine serum and antibiotics (1% penicillin and streptomycin). Serum-starved cells were stimulated with with unclustered or pre-clustered mouse EphrinB2-Fc-His (to stimulate forward signaling) or mouse EphB2-Fc-His (to stimulate reverse signaling) in protein free DMEM or DMEM/F12 supplemented with 10 mM HEPES. For pre-clustering, selected Fc protein was combined with goat anti-human IgG at a 2:1 ratio for at least 1 hr prior to cell stimulations. Following stimulations, plates were placed on ice, cells washed with cold PBS, and then lysed using 1 ml/well ice cold PLC Lysis Buffer (50mM HEPES (pH 7.5), 150mM NaCl, 1.5mM MgCl2, 10% Glycerol, 1% Triton-X100, 1 mM EGTA, 10 mM Na4P2O7 .10H2O, 10 mM NaF, 1 mM

Na3VO4, 1X Halt Protease Inhibitor Cocktail, 1 mM PMSF). After Nutating the lysate for 30 min in a cold room, the insoluble material was pelleted, and cleared supernatants frozen on dry ice and placed in -80 freezer for long-term storage.

Protein lysates from ground frozen powders of mouse tissues (embryos, brains, intestines, kidneys) were made by dounce homogenization in ice cold PLC Lysis Buffer (3 ml PLC lysis buffer for every 0.1 g of ground tissue powder). After Nutating the lysate for 60 min in a cold room, the insoluble material was pelleted, and 1 ml aliquots of cleared supernatant frozen on dry ice and placed in -80 freezer for long-term storage.

In vitro kinase assay

Frozen protein lysates (1 ml) prepared in advance from mouse embryo or brain tissues were thawed on ice and 1 ug of goat anti-EphB2 antibody and 20 ul of washed G sepharose bead slurry added to immunoprecipitate the receptor protein. Beads were washed 3X in ice cold HNTGV (20 mM HEPES pH 7.5, 150 mM NaCl, 1% Triton-X100, 10% Glycerol, 1 mM Na3VO4), washed briefly in 1X Kinase Buffer (20 mM HEPES pH 7.5, 10 mM MgCl2, 4 mM MnCl2, 0.1 mM Na3VO4), and then incubated at room temperature RT for 15 minutes in 45 ul of 1X Kinase Buffer containing 200 μM ATP. Kinase reaction was terminated by adding 15 μl 6X SDS Sample Buffer containing DTT and heating at 65°C for 5 minutes, proteins resolved on SDS-PAGE gels, transferred to membranes, and immunoblotted with indicated antibodies.

Phosphotyrosine quantification

Frozen protein lysates (1 ml) prepared in advance from desired source (mouse embryo, brain, intestine, kidney, Cos1/stellate cells) were thawed on ice and after removing a small sample for the immunoblot lysate lanes either 1 ug of desired anti-phosphotyrosine antibody and 20 ul of washed Protein G Sepharose bead slurry or 20 ul of bead-conjugated pTyr1000 antibody or bead-conjugated SH2 superbinder domain were added and allowed to Nutate in a cold room for 2 hr to immunoprecipitate phosphotyrosine-containing proteins. Beads were washed 3X in ice cold low salt HNTGV (20 mM HEPES, pH 7.5, 50 mM NaCl, 0.02% Triton-X100, 10% Glycerol, 1 mM Na3VO4), and proteins eluted by adding 15 μl 6X SDS Sample Buffer containing DTT and heating at 65°C for 5 minutes, then resolved on SDS-PAGE gels, transferred to membranes, and immunoblotted with indicated antibodies.

Animal studies

All animal procedures were approved by the Institutional Animal Care and Use Committee at UT Southwestern Medical Center (IACUC Protocol #2016-101651).

CFA pain. In the week prior to beginning a study, mice were first acclimated to the chambers used in pain assessments and their left and right hind paws were subjected to thermal (heat) and mechanical (touch) pain measurements to obtain baseline data. Thermal pain was assessed by placing mice on a glass surface and subjecting their hind paws to an infrared heat source (Hargreaves device, Ugo Basile) that is connected to a timer to measure how long the animal takes to notice the heat and lift the paw. Mechanical pain was assessed by placing mice on a wire grid and repeatably testing hind paws for their sensitivity to a set of 20 von Frey (VF) monofilaments of different stiffnesses (Bioseb Instruments) with the mechanical withdrawal threshold for each mouse hind paw defined as the minimum gauge filament needed to elicit a reflex. In these tests, both hind paws of mice were subjected to multiple measurements over a 2-3 hr period to (1) obtain 6-8 good thermal response measurements which are averaged to provide the data points for heat pain or (2) narrow down the VF filament stiffness threshold to plot the touch pain. Chronic pain was initiated by subcutaneously injecting 30 µl of CFA (Sigma-Aldrich, F5881) into the plantar surface of the left hind paws to induce inflammatory pain. In subsequent days mice were then tested for either thermal or mechanical pain responses as indicated up to 15 days. In all of the experiments, the person doing the actual pain testing of mice was kept blinded to the mouse genotypes (e.g. wild-type or *EphB1* knockout) and/or treatment conditions (e.g. vehicle only or dosed with an A20 chemical). Up to 12 mice were assessed in any one experiment. Thermal pain ratios were calculated by dividing the average response of uninjured right paw by the average response obtained from the injured left paw. Mechanical pain ratios were calculated by dividing the VF response of uninjured right paw by the VF response obtained from the injured left paw.

Zymosan pain. Mice were first acclimated to the chambers used in pain assessments and their left hind paws were subjected to thermal (heat) and mechanical (touch) pain measurements to obtain baseline data. On a subsequent day, the plantar surface of the left hind paws were injected subcutaneously with 30 µl of 5 mg/ml Zymosan (Sigma-Aldrich, Z4250) dissolved in PBS and then assessed for thermal pain using Hargreaves device (2-4 hr), for mechanical pain using VF filaments (4-6 hr), and then again for thermal pain (6-8 hr). In some experiments, mechanical pain was assessed first (2-4 hr),

followed by tests for thermal pain (4-6 hr), and then again for mechanical pain (6-8 hr). Pain ratios were calculated by dividing the response of left paw obtained during baseline (uninjured) measurements by the response obtained from the same hind paw post-Zymosan (injured).

DH neurons. Mice bred to contain the *Trap2-CreERT2* driver and the *Ai9-tdTomato* reporter were injected with CFA to induce inflammatory pain. Four hours later, mice were then injected IP with 40 mg/kg 4-hydroxytamoxifen (4-OHT) (Hello Bio, HB6040) dissolved in sunflower seed oil) to activate Cre recombinase and permanently label with red fluorescence the neurons that were activated during the short window of time (~8 hr) until the 4-OHT is degraded. Fourteen days later, animals were perfused with 4% paraformaldehyde dissolved in PBS and then 50 μm thick vibratome serial sections throughout the lumbar spinal cord were obtained, slices mounted, and then viewed under fluorescence microscopy to identify and image red labeled neurons in the superficial dorsal horn of the spinal cords that were activated between ~4-12 hr after the CFA induction of inflammatory pain. Superficial red neurons were counted on the left (injured) and right (uninjured) side dorsal horns from 8-12 sections along the span of lumbar cord of each animal. The ratio of Trap2+ activated neurons for each animal was then determined by dividing the average number of red neurons from the injured side by the number obtained from the uninjured side.

Morphine withdrawal. Mice were injected intraperitoneally (IP) with increasing morphine doses in normal saline every 12 hr for 4 consecutive days (day 1: 20 mg/kg, day 2: 40 mg/kg, day 3: 60 mg/kg, day 4: 80 mg/kg) and on the fifth day in the morning they were injected with a final 100 mg/kg morphine dose which was staggered by one mouse every 30 minutes. Exactly 3 hr after the last morphine injection, each mouse was weighed, and withdrawal precipitated using naloxone hydrochloride that was subcutaneously injected at 1 mg/kg. Withdrawal signs were then monitored by an examiner who was blinded to animal genotypes or treatment groups for 30 min after naloxone administration to identify the number of jumps, wet dog shakes, and diarrhea events observed in the 30 min period, and % change in weight from before naloxone administration to 30 min post withdrawal. For tremor and ptosis, the presence of tremor and/or a drooping upper eyelid is monitored at the beginning of each 5 min interval during the 30 min monitoring period.

Statistics and reproducibility

Statistical analysis (t-test, one-way ANOVA, and two-way ANOVA) was done using GraphPad software v.10.6.1 (799). The tests used are noted in the figure legends. All tests are two sided and unpaired. A significance level of 0.05 was used to reject the null hypothesis. The sample size, age and sex of experimental animals, as well as the summary of each statistical test (including degrees of freedom, confidence intervals and P values) can be found in the Figures, associated legends, Extended Data Figures, and Supplementary Tables 3-6. All animal experiments were done using biologically independent samples (individual animals) with each data point plotted on scatter graphs unless noted. Representative immunolabelling images shown are from one animal per group, selected from multiple animals that consistently showed similar results.

Computer programs

Find50.py Was developed to analyze biophysical kinetic data generated by the Octet RED384 instrument and calculate (1) the % of a protein-protein interaction that is inhibited at a given concentration of an inhibitor and (2) the IC_{50} value of an inhibitor using area under the curve (AUC) analysis. Find50.py can also be utilized with other types of dose/concentration-dependent data that generates curves needing AUC analysis and IC_{50} calculations. If an accurate K_D is known, FIND50.py will further use the calculated IC_{50} value and concentration of the soluble protein used to determine IC_{50} [L], to calculate the K_i (inhibition constant) using the Cheng-Prussof equation: $K_i = IC_{50}/(1+ [L]/K_D)$. The K_i is a dissociation constant specific for the protein-inhibitor complex; a lower value indicates a stronger binding affinity as it indicates a lower concentration of the competitive inhibitor is needed to occupy 50% of its target protein. This equation defines the theoretical relationship between the IC_{50} and K_i of an inhibitory compound based on the K_D of the interaction it is inhibiting and provides a useful constant to describe a specific inhibitor's activity towards its target.

EasyCellCounting.py Was developed to count and quantify labeled cells from microscope images within a selected area of interest to the end user. EasyCellCounting.py can be used with precision for any type of cell labeling system, as long as signal-to-noise ratios are discernible over background levels, and it is particularly useful for counting images of fluorescent labeled cells. EasyCellCounting.py was developed to replace the labor-intensive manual process of

counting Tom+ red fluorescent neurons in the spinal cord with a highly optimized and efficient program, though the program should be of broad use to anyone needing to count and quantify cell numbers no matter what was used to label them. Further, EasyCellCounting.py eliminates bias and increases the overall precision of counting cells compared to manual counting.

Proteins

Recombinant Eph/Ephrin ectodomain proteins:

Human Fc protein (R&D Systems, 110-HG-100). Is a 26.6 kDa protein (with human Fc Pro100-Lys330) that migrates as a 30-35 kDa protein in SDS-PAGE under reducing conditions.

Rat EphB1-Fc protein (R&D Systems, 1596-B1-200). Is an 85 kDa Fc fusion protein (with rat EphB1: Met18-Gln538) that migrates as a 102 kDa protein in SDS-PAGE under reducing conditions.

Mouse EphB2-Fc-His protein (R&D Systems, 467-B2-200). Is an 85 kDa Fc fusion protein (with mouse EphB2: Val27-Lys548) that migrates as a 100-110 kDa protein in SDS-PAGE under reducing conditions.

Human EphB4-Fc (R&D Systems, 11307-B4). Is an 85.2 kDa fusion Fc protein (with human EphB4: Leu16-Arg539) that migrates as a 95-108 kDa protein in SDS-PAGE under reducing conditions.

Human EphA3-Fc (R&D Systems, 6444-A3-050). Is an 85.4 kDa Fc fusion protein (with human EphA3: Met1-Gln541) that migrates as a 100-110 kDa protein in SDS-PAGE under reducing conditions.

Human EphrinB1-Fc (R&D Systems, 7654-EB-050). Is a 49.5 kDa Fc fusion protein (with human EphrinB1: Leu28-Ser236) that migrates as a 62-67 kDa protein in SDS-PAGE under reducing conditions.

Mouse EphrinB2-Fc-His protein (R&D Systems, 496-EB-200). Is a 49.6 kDa Fc-His fusion protein (with mouse EphrinB2: Arg27-Ala227) that migrates as a 60-65 kDa protein in SDS-PAGE under reducing conditions.

Human EphrinB2-Fc (R&D Systems, 7397-EB-050). Is a 48.8 kDa Fc fusion protein (with human EphrinB2: Met1-Ala229) that migrates as a 58-66 kDa protein in SDS-PAGE under reducing conditions.

Human EphrinB3-Fc (R&D Systems, 7924-EB-050). Is a 48.3 kDa Fc fusion protein (with human EphrinB3: Leu28-Ser224) that migrates as a 57-61 kDa protein in SDS-PAGE under reducing conditions.

Human EphB1-His (Sino Biologicals, 11963-H08H). Is a 60 kDa His fusion protein (human EphB1: Met1-Pro540) that migrates as a 66 kDa protein in SDS-PAGE under reducing conditions.

Human EphB2-His (Sino Biologicals, 10762-H08H). Is a 59.7 kDa His fusion protein (human EphB2: Met1-Leu543) that migrates as a 70 kDa protein in SDS-PAGE under reducing conditions.

Human EphB4-His (Sino Biologicals, 10235-H08H). Is a 58.5 kDa His fusion protein (human EphB4: Met1-Ala539) that migrates as a 72 kDa protein in SDS-PAGE under reducing conditions.

Mouse EphrinB1-His protein (Sino Biologicals, 50580-M08H). Is a 23.3 kDa His fusion protein (with mouse EphrinB1: Met1-Ser229) that migrates as a 33-38 kDa protein in SDS-PAGE under reducing conditions.

Mouse EphrinB2-His protein (Sino Biologicals, 50598-M08H). Is a 23.5 kDa His fusion protein (with mouse EphrinB2: Met1-Ala232) that migrates as a 30-40 kDa protein in SDS-PAGE under reducing conditions.

Rat EphrinB2-His protein (Sino Biologicals, 80107-R08H). Is a 23.5 kDa His fusion protein (with rat EphrinB2: Met1-Ala229) that migrates as a 33-39 kDa protein in SDS-PAGE under reducing conditions.

Human EphrinB2-His protein (Sino Biologicals, 10881-H08H). Is a 23.5 kDa His fusion protein (with human EphrinB2: Met1-Ala229) that migrates as a 35-40 kDa protein in SDS-PAGE under reducing conditions.

Human EphrinA1-His protein (Sino Biologicals, 10882-H08H). Is a 20.8 kDa His fusion protein (with mouse EphrinA1: Met1-Ser182) that migrates as a 26 kDa protein in SDS-PAGE under reducing conditions.

Human EphrinA5-His protein (Sino Biologicals, 10192-H08H). Is a 23 kDa His fusion protein (with mouse EphrinA1: Met1-Asn203) that migrates as a 27 kDa protein in SDS-PAGE under reducing conditions.

Primary Antibodies and phosphotyrosine detection reagents:
Goat anti-EphB2 antibody (R&D Systems, AF467). Polyclonal antibody raised against mouse EphB2 ectodomain Val27-Lys548. Recognizes both unphosphorylated EphB2 band (<130 kDa) and tyrosine phosphorylated pEphB2 (>130 kDa).

Rabbit anti-EphB2 antibody [D2X2I] (Cell Signaling, 83029). Monoclonal antibody raised against an unphosphorylated intracellular peptide corresponding to juxtamembrane residues surrounding Ala573 of human EphB2 protein, just after the TM segment. Only recognizes the unphosphorylated EphB2 protein (<130 kDa).

Rabbit anti-phospho-EphB1/2 (Abcam, 61791). Polyclonal antibody raised against the conserved tyrosine phosphorylated intracellular juxtamembrane peptide at residue pY594 in EphB1 and pY596 in EphB2 protein (pYIDP). Only recognizes the tyrosine phosphorylated EphB2 protein (>130 kDa).

Goat anti-EphrinB2 (R&D Systems, AF496). Polyclonal antibody raised against mouse EphrinB2 ectodomain Arg27-Ala227. Recognizes both unphosphorylated EphrinB2 in a broad band (35-50 kDa) and tyrosine phosphorylated pEphrinB2 (40-50 kDa)..

Rabbit anti-phosphotyrosine MultiMab™ Rabbit mAb mix (pTyr1000) (Cell Signaling, 8954). A mixture of rabbit monoclonal antibodies that recognizes a broad range of tyrosine-phosphorylated proteins and peptides, and does not cross-react with proteins or peptides containing phospho-Ser or phospho-Thr residues.

4G10® Platinum anti-phosphotyrosine Antibody (mouse monoclonal cocktail IgG2b) (Millipore Sigma, 05-1050). A mixture of mouse 4G10 and PY20 monoclonal antibodies that recognizes a broad range of tyrosine-phosphorylated proteins.

Rabbit anti-phosphotyrosine MultiMab™ Rabbit mAb mix (pTyr1000 / Sepharose Bead Conjugate) (Cell Signaling, 14005). A mixture of rabbit monoclonal antibodies that recognizes a broad range of tyrosine-phosphorylated proteins and peptides conjugated to sepharose beads for use in immunoprecipitations.

SH2 Superbinder (SH2S) Agarose Conjugate (Precision Proteomics, PPI-001). The SH2 Superbinder (SH2S) is an engineered SH2 domain protein conjugated to agarose beads that binds to phosphotyrosine containing proteins with antibody-like affinity. The SH2 superbinder beads may be used like an anti-phosphotyrosine antibody in numerous applications, including immunoprecipitation and affinity purification to measure global or target protein tyrosine phosphorylation.

Secondary Antibodies and detection reagents:
Bovine anti-Goat HRP secondary:(Jackson ImmunoResearch, 805-035-180). Peroxidase AffiniPure Bovine Anti-Goat IgG (H+L) (min X Bov, Ck, GP, Sy Hms, Hrs, Hu, Ms, Rb, Rat Sr Prot).

Goat anti-Rabbit HRP secondary (Jackson ImmunoResearch, 111-035-144). Peroxidase AffiniPure Goat Anti-Rabbit IgG (H+L) (min X Hu, Ms, Rat Sr Prot).

Donkey anti-Mouse HRP secondary (Jackson ImmunoResearch, 715-035-151). Peroxidase AffiniPure Donkey Anti-Mouse IgG (H+L) (min X Bov, Ck, Gt, GP, Sy Hms, Hrs, Hu, Rb, Rat, Shp Sr Prot).

6xHis Tag (C-term) Monoclonal Antibody (3D5), HRP conjugated (Thermo Scientific, R931-25). Used to detect His-tagged recombinant proteins.

Mouse Penta·His Antibody (Qiagen, 34660). A combination of mouse monoclonal anti·His antibodies used to detect His-tagged recombinant proteins.

Peroxidase AffiniPure Goat Anti-Human IgG, Fcγ fragment specific (Jackson ImmunoResearch, 109-035-098). A polyclonal anti-Fc antibody used to detect Fc-tagged recombinant proteins.

AffiniPure® Goat Anti-Human IgG, Fcγ fragment specific (Jackson ImmunoResearch, 109-005-008). A polyclonal anti-Fc antibody used to pre-cluster EphrinB2-Fc and EphB2-Fc ectodomain proteins for cell stimulations.

ELISA Pico Chemiluminescent Substrate (Thermo Scientific, 37069). ELISA Pico Chemiluminescent Substrate is optimized to generate an intense light signal and provide exceptional performance in luminometer-based assays.

SuperSignal West Dura Extended Duration Substrate (Thermo Scientific, 34076). A luminol-based enhanced chemiluminescence (ECL) horseradish peroxidase (HRP) substrate ideal for quantitative western blotting with stable light output for mid-femtogram level detection for western blot analysis.

Acknowledgements We thank our colleagues at UT Southwestern for valuable use of instutitionally supported core facilities, technicial assistance, and discussion: Bruce Posner, Shuguang Wei, and Prema Latha Mallipeddi (HTS Core), Chad A. Brautigam and Shih-Chia Tso (Macromolecular Biophysics Resource Core), Noelle Williams (Preclinical Pharmacology Core), and Sherry Birnbaum (Rodent Behavior Core). We also thank Marc Diamond for generous use of the Octet RED384 instrument available in his laboratory, Joachim Herz for recombinant Reelin protein, and Cerian Bolton, Edward Carter, and Richard Grose at the Barts Cancer Institute - Queen Mary University of London for pancreatic stellate cells. Patrice Mimche, Dean Sherry, Hesham Sadek, Nick Carruthers, Tracy Saxton, Chad Cowan, and Derrick Rossi provided valuable discussions. The HTS core facility was supported by NIH awards for Cancer Center Support 2P30CA142543-16 and Instrumentation 1S10OD026758-01, and the mass photometer in the Macromolecular Biophysics Resource Core was supported by S10OD030312-01. A.K. was supported in part by a Herchel Smith summer fellowship. This research was made possible by DOD / U.S. Army Medical Research and Development Command awards W81XWH-14-1-0220 and W81XWH-21-1-0949 (to M.H), and NIH award R01DK128819 (to M.H. and P.M.).

Author contributions H.W. performed chemical synthesis, DH neuron analysis, and assisted with other aspects of the study, A.K. performed chemical synthesis, biophysical studies, DH neuron analysis, and wrote computer programs, F.S. was lab manager, preformed biochemistry, DH neuron analysis, and helped with animals and pain studies, M.K. did the HTS screen and early work on A20 chemicals, K.C. conducted the pain behavioral testing, E.B. performed biophysical studies, T.K. performed biochemistry, A.T. conducted the cell clustering experiment, M.S.A. performed chemical synthesis, C.M.U.G. performed chemical synthesis, Alpha assays, and mass photometry, M.O. performed chemical synthesis, M.H. conducted numerous experiments throughout the study, supervised and guided all aspects of the work, and wrote the manuscript with input from the other authors.

Competing interests M.H. recently founded a company, Ephius Texas, Inc. that is dedicated to the clinical translation of this technology.

References

1 Bush, J. O. Cellular and molecular mechanisms of EPH/EPHRIN signaling in evolution and development. *Curr Top Dev Biol* **149**, 153-201 (2022). https://doi.org/10.1016/bs.ctdb.2022.02.005

2 Pasquale, E. B. Eph receptor signaling complexes in the plasma membrane. *Trends Biochem Sci* **49**, 1079-1096 (2024). https://doi.org/10.1016/j.tibs.2024.10.002

3 Himanen, J. P. *et al.* Crystal structure of an Eph receptor-ephrin complex. *Nature* **414**, 933-938. (2001).

4 Henkemeyer, M. *et al.* Nuk controls pathfinding of commissural axons in the mammalian central nervous system. *Cell* **86**, 35-46 (1996). https://doi.org/10.1016/s0092-8674(00)80075-6

5 Holland, S. J. *et al.* Bidirectional signalling through the EPH-family receptor Nuk and its transmembrane ligands. *Nature* **383**, 722-725 (1996). https://doi.org/10.1038/383722a0

6 Cowan, C. A. & Henkemeyer, M. The SH2/SH3 adaptor Grb4 transduces B-ephrin reverse signals. *Nature* **413**, 174-179. (2001).

7 Pasquale, E. B. Eph-ephrin bidirectional signaling in physiology and disease. *Cell* **133**, 38-52 (2008). https://doi.org/10.1016/j.cell.2008.03.011

8 Kania, A. & Klein, R. Mechanisms of ephrin-Eph signalling in development, physiology and disease. *Nat Rev Mol Cell Biol* **17**, 240-256 (2016). https://doi.org/10.1038/nrm.2015.16

9 Pasquale, E. B. Eph receptors and ephrins in cancer progression. *Nat Rev Cancer* **24**, 5-27 (2024). https://doi.org/10.1038/s41568-023-00634-x

10 Wu, B., Rockel, J. S., Lagares, D. & Kapoor, M. Ephrins and Eph Receptor Signaling in Tissue Repair and Fibrosis. *Curr Rheumatol Rep* **21**, 23 (2019). https://doi.org/10.1007/s11926-019-0825-x

11 Lagares, D. *et al.* ADAM10-mediated ephrin-B2 shedding promotes myofibroblast activation and organ fibrosis. *Nat Med* **23**, 1405-1415 (2017). https://doi.org/10.1038/nm.4419

12 Huang, Z. *et al.* Key role for EphB2 receptor in kidney fibrosis. *Clin Sci (Lond)* **135**, 2127-2142 (2021). https://doi.org/10.1042/CS20210644

13 Egal, E. S. A. *et al.* EphB2 Receptor Promotes Dermal Fibrosis in Systemic Sclerosis. *Arthritis Rheumatol* **76**, 1303-1316 (2024). https://doi.org/10.1002/art.42858

14 Jiang, X., Wang, W. & Kang, H. EPHB2 Knockdown Mitigated Myocardial Infarction by Inhibiting MAPK Signaling. *Adv Biol (Weinh)* **8**, e2300517 (2024). https://doi.org/10.1002/adbi.202300517

15 Yoshigi, M. *et al.* EPHB2 deficiency suppresses liver fibrosis in metabolic dysfunction-associated steatohepatitis. (submitted).

16 Hoang, S. A. *et al.* Gene Expression Predicts Histological Severity and Reveals Distinct Molecular Profiles of Nonalcoholic Fatty Liver Disease. *Sci Rep* **9**, 12541 (2019). https://doi.org/10.1038/s41598-019-48746-5

17 Wang, S. *et al.* An autocrine signaling circuit in hepatic stellate cells underlies advanced fibrosis in nonalcoholic steatohepatitis. *Sci Transl Med* **15**, eadd3949 (2023). https://doi.org/10.1126/scitranslmed.add3949
18 Xiao, Y. *et al.* Hepatocytes demarcated by EphB2 contribute to the progression of nonalcoholic steatohepatitis. *Sci Transl Med* **15**, eadc9653 (2023). https://doi.org/10.1126/scitranslmed.adc9653
19 Yang, J. S., Wei, H. X., Chen, P. P. & Wu, G. Roles of Eph/ephrin bidirectional signaling in central nervous system injury and recovery. *Exp Ther Med* **15**, 2219-2227 (2018). https://doi.org/10.3892/etm.2018.5702
20 Modi, A. *et al.* Disentangling the enigmatic role of ephrin signaling in chronic pain: Moving towards future anti-pain therapeutics. *Life Sci* **326**, 121796 (2023). https://doi.org/10.1016/j.lfs.2023.121796
21 Ma, P. *et al.* Activation of EphB receptors contributes to primary sensory neuron excitability by facilitating Ca2+ influx directly or through Src kinase-mediated N-methyl-D-aspartate receptor phosphorylation. *Pain* **161**, 1584-1596 (2020). https://doi.org/10.1097/j.pain.0000000000001855
22 David, E. T. *et al.* ephrin-B2 promotes nociceptive plasticity and hyperalgesic priming through EphB2-MNK-eIF4E signaling in both mice and humans. *Pharmacol Res* **206**, 107284 (2024). https://doi.org/10.1016/j.phrs.2024.107284
23 Han, Y., Song, X. S., Liu, W. T., Henkemeyer, M. & Song, X. J. Targeted mutation of EphB1 receptor prevents development of neuropathic hyperalgesia and physical dependence on morphine in mice. *Mol Pain* **4**, 60 (2008). https://doi.org/1744-8069-4-60 [pii] 10.1186/1744-8069-4-60
24 Song, X. J. *et al.* Upregulation and redistribution of ephrinB and EphB receptor in dorsal root ganglion and spinal dorsal horn neurons after peripheral nerve injury and dorsal rhizotomy. *Eur J Pain* **12**, 1031-1039 (2008). https://doi.org/S1090-3801(08)00019-0 [pii] 10.1016/j.ejpain.2008.01.011
25 Liu, W. T. *et al.* An in vivo mouse model of long-term potentiation at synapses between primary afferent C-fibers and spinal dorsal horn neurons: essential role of EphB1 receptor. *Mol Pain* **5**, 29 (2009). https://doi.org/1744-8069-5-29 [pii] 10.1186/1744-8069-5-29
26 Zhao, J. *et al.* Nociceptor-expressed ephrin-B2 regulates inflammatory and neuropathic pain. *Mol Pain* **6**, 77 (2010). https://doi.org/1744-8069-6-77 [pii] 10.1186/1744-8069-6-77
27 Liu, S. *et al.* Blocking EphB1 receptor forward signaling in spinal cord relieves bone cancer pain and rescues analgesic effect of morphine treatment in rodents. *Cancer Res* **71**, 4392-4402 (2011). https://doi.org/10.1158/0008-5472.CAN-10-3870
28 Cibert-Goton, V. *et al.* Involvement of EphB1 receptors signalling in models of inflammatory and neuropathic pain. *PLoS One* **8**, e53673 (2013). https://doi.org/10.1371/journal.pone.0053673 PONE-D-12-21867 [pii]
29 Dalva, M. B. *et al.* EphB receptors interact with NMDA receptors and regulate excitatory synapse formation. *Cell* **103**, 945-956. (2000).
30 Takasu, M. A., Dalva, M. B., Zigmond, R. E. & Greenberg, M. E. Modulation of NMDA receptor-dependent calcium influx and gene expression through EphB receptors. *Science* **295**, 491-495. (2002).

31 Li, R. W. *et al.* Dramatic regulation of heparanase activity and angiogenesis gene expression in synovium from patients with rheumatoid arthritis. *Arthritis Rheum* **58**, 1590-1600 (2008). https://doi.org/10.1002/art.23489
32 Bai, Z. *et al.* Synovial fibroblast gene expression is associated with sensory nerve growth and pain in rheumatoid arthritis. *Sci Transl Med* **16**, eadk3506 (2024). https://doi.org/10.1126/scitranslmed.adk3506
33 Kitamura, T. *et al.* Enhancement of lymphocyte migration and cytokine production by ephrinB1 system in rheumatoid arthritis. *Am J Physiol Cell Physiol* **294**, C189-196 (2008). https://doi.org/10.1152/ajpcell.00314.2007
34 Hall, B. E. *et al.* Transcriptomic analysis of human sensory neurons in painful diabetic neuropathy reveals inflammation and neuronal loss. *Sci Rep* **12**, 4729 (2022). https://doi.org/10.1038/s41598-022-08100-8
35 Toikumo, S. *et al.* Etiological basis for chronic pain genetic variation in brain and dorsal root ganglia cell types. *medRxiv* (2025). https://doi.org/10.1101/2025.07.03.25330832
36 Henkemeyer, M., Itkis, O. S., Ngo, M., Hickmott, P. W. & Ethell, I. M. Multiple EphB receptor tyrosine kinases shape dendritic spines in the hippocampus. *J Cell Biol* **163**, 1313-1326 (2003).
37 Ahmed, M. S. *et al.* Identification of tetracycline combinations as EphB1 tyrosine kinase inhibitors for treatment of neuropathic pain. *Proc Natl Acad Sci U S A* **118** (2021). https://doi.org/10.1073/pnas.2016265118
38 Himanen, J. P. *et al.* Repelling class discrimination: ephrin-A5 binds to and activates EphB2 receptor signaling. *Nat Neurosci* **7**, 501-509 (2004).
39 Koolpe, M., Burgess, R., Dail, M. & Pasquale, E. B. EphB receptor-binding peptides identified by phage display enable design of an antagonist with ephrin-like affinity. *J Biol Chem* **280**, 17301-17311 (2005).
40 Bouche, E. *et al.* Reelin induces EphB activation. *Cell Res* **23**, 473-490 (2013). https://doi.org/10.1038/cr.2013.7 cr20137 [pii]
41 Henkemeyer, M. *et al.* Immunolocalization of the Nuk receptor tyrosine kinase suggests roles in segmental patterning of the brain and axonogenesis. *Oncogene* **9**, 1001-1014 (1994).
42 Williams, S. E. *et al.* Ephrin-B2 and EphB1 mediate retinal axon divergence at the optic chiasm. *Neuron* **39**, 919-935 (2003).
43 Holmberg, J. *et al.* EphB receptors coordinate migration and proliferation in the intestinal stem cell niche. *Cell* **125**, 1151-1163 (2006).
44 Genander, M. *et al.* Dissociation of EphB2 signaling pathways mediating progenitor cell proliferation and tumor suppression. *Cell* **139**, 679-692 (2009). https://doi.org/S0092-8674(09)01188-X [pii] 10.1016/j.cell.2009.08.048
45 Chenaux, G. & Henkemeyer, M. Forward signaling by EphB1/EphB2 interacting with ephrin-B ligands at the optic chiasm is required to form the ipsilateral projection. *Eur J Neurosci* **34**, 1620-1633 (2011). https://doi.org/10.1111/j.1460-9568.2011.07845.x
46 Khambete, A., Wang, W. & Henkemeyer, M. Eph-Ephrin tetramerization is driven by a high-affinity copper-binding like proteinaceous chelator activity. (submitted).

47 Dravis, C. *et al.* Bidirectional signaling mediated by ephrin-B2 and EphB2 controls urorectal development. *Dev Biol* **271**, 272-290 (2004). https://doi.org/10.1016/j.ydbio.2004.03.027
48 Dravis, C. & Henkemeyer, M. Ephrin-B reverse signaling controls septation events at the embryonic midline through separate tyrosine phosphorylation-independent signaling avenues. *Dev Biol* **355**, 138-151 (2011). https://doi.org/10.1016/j.ydbio.2011.04.020
49 Madisen, L. *et al.* A robust and high-throughput Cre reporting and characterization system for the whole mouse brain. *Nat Neurosci* **13**, 133-140 (2010). https://doi.org/10.1038/nn.2467
50 DeNardo, L. A. *et al.* Temporal evolution of cortical ensembles promoting remote memory retrieval. *Nat Neurosci* (2019). https://doi.org/10.1038/s41593-018-0318-7
51 Liu, W. T., Li, H. C., Song, X. S., Huang, Z. J. & Song, X. J. EphB receptor signaling in mouse spinal cord contributes to physical dependence on morphine. *FASEB J* **23**, 90-98 (2009). https://doi.org/fj.08-114462 [pii] 10.1096/fj.08-114462
52 Glass, M. J. Opioid dependence and NMDA receptors. *ILAR J* **52**, 342-351 (2011). https://doi.org/10.1093/ilar.52.3.342
53 Bolton, C. L. *et al.* Ephrin inhibition disrupts stromal-cancer crosstalk and reduces metastasis in pancreatic cancer. (submitted).
54 Contractor, A. *et al.* Trans-synaptic Eph receptor-ephrin signaling in hippocampal mossy fiber LTP. *Science* **296**, 1864-1869. (2002).
55 Noberini, R. *et al.* Small molecules can selectively inhibit ephrin binding to the EphA4 and EphA2 receptors. *J Biol Chem* **283**, 29461-29472 (2008). https://doi.org/M804103200 [pii] 10.1074/jbc.M804103200
56 Qin, H., Shi, J., Noberini, R., Pasquale, E. B. & Song, J. Crystal structure and NMR binding reveal that two small molecule antagonists target the high affinity ephrin-binding channel of the EphA4 receptor. *J Biol Chem* **283**, 29473-29484 (2008). https://doi.org/M804114200 [pii] 10.1074/jbc.M804114200
57 Noberini, R. *et al.* A disalicylic acid-furanyl derivative inhibits ephrin binding to a subset of Eph receptors. *Chem Biol Drug Des* **78**, 667-678 (2011). https://doi.org/10.1111/j.1747-0285.2011.01199.x
58 Tognolini, M. *et al.* Structure-activity relationships and mechanism of action of Eph-ephrin antagonists: interaction of cholanic acid with the EphA2 receptor. *ChemMedChem* **7**, 1071-1083 (2012). https://doi.org/10.1002/cmdc.201200102
59 Castelli, R. *et al.* Delta(5)-Cholenoyl-amino acids as selective and orally available antagonists of the Eph-ephrin system. *Eur J Med Chem* **103**, 312-324 (2015). https://doi.org/10.1016/j.ejmech.2015.08.048
60 Tognolini, M. & Lodola, A. Targeting the Eph-ephrin System with Protein-Protein Interaction (PPI) Inhibitors. *Curr Drug Targets* **16**, 1048-1056 (2015). https://doi.org/10.2174/1389450116666150825144457
61 Guidetti, L. *et al.* Protein-Protein Interaction Inhibitors Targeting the Eph-Ephrin System with a Focus on Amino Acid Conjugates of Bile Acids. *Pharmaceuticals (Basel)* **15** (2022). https://doi.org/10.3390/ph15020137

62 Chrencik, J. E. *et al.* Structural and biophysical characterization of the EphB4*ephrinB2 protein-protein interaction and receptor specificity. *J Biol Chem* **281**, 28185-28192 (2006). https://doi.org/10.1074/jbc.M605766200
63 Chrencik, J. E. *et al.* Structure and thermodynamic characterization of the EphB4/Ephrin-B2 antagonist peptide complex reveals the determinants for receptor specificity. *Structure* **14**, 321-330 (2006).
64 Gerety, S. S., Wang, H. U., Chen, Z. F. & Anderson, D. J. Symmetrical mutant phenotypes of the receptor EphB4 and its specific transmembrane ligand ephrin-B2 in cardiovascular development. *Mol Cell* **4**, 403-414 (1999).
65 Gerety, S. S. & Anderson, D. J. Cardiovascular ephrinB2 function is essential for embryonic angiogenesis. *Development* **129**, 1397-1410 (2002).
66 Erber, R. *et al.* EphB4 controls blood vascular morphogenesis during postnatal angiogenesis. *EMBO J* **25**, 628-641 (2006). https://doi.org/10.1038/sj.emboj.7600949
67 Du, E., Li, X., He, S., Li, X. & He, S. The critical role of the interplays of EphrinB2/EphB4 and VEGF in the induction of angiogenesis. *Mol Biol Rep* **47**, 4681-4690 (2020). https://doi.org/10.1007/s11033-020-05470-y
68 Adams, R. H. *et al.* Roles of ephrinB ligands and EphB receptors in cardiovascular development: demarcation of arterial/venous domains, vascular morphogenesis, and sprouting angiogenesis. *Genes and Dev.* **13**, 295-306 (1999).
69 Zhi, X. *et al.* Small interfering RNA drug knockdown of EphrinB3 attenuates neuropathic pain after spinal cord injury in rats. *African Journal of Pharmacy and Pharmacology* **6**, 3215-3220 (2012).
70 Leem, A. Y. *et al.* All-trans retinoic acid attenuates bleomycin-induced pulmonary fibrosis via downregulating EphA2-EphrinA1 signaling. *Biochem Biophys Res Commun* **491**, 721-726 (2017). https://doi.org/10.1016/j.bbrc.2017.07.122
71 Hohmann, M. S. *et al.* Antibody-mediated depletion of CCR10+EphA3+ cells ameliorates fibrosis in IPF. *JCI Insight* **6** (2021). https://doi.org/10.1172/jci.insight.141061

Figure Legends

Fig. 1. Discovery of small molecules that disrupt the high-affinity Eph-Ephrin tetramer.

a, Transmembrane EphB receptors and EphrinB ligands interact to form dimers, tetramers, and tetramer clusters at sites of cell-cell contact to activate bidirectional signaling. While not shown, forward signaling by EphB receptors is driven by activation of their intracellular tyrosine kinase catalytic domain, autophosphorylation of key juxtamembrane tyrosine residues, and coupling to intracellular SH2 and PDZ domain proteins, while reverse signaling by EphrinB ligands involves phosphorylation of conserved tyrosine residues on their short intracellular tail and coupling to SH2 and PDZ domain proteins.

b, Shown are BLI sensorgram traces obtained from AHC sensorchip immobilized human EphrinB1-Fc, EphrinB2-Fc, and EphrinB3-Fc ectodomains binding to 50 nM soluble human EphB1-His, EphB2-His, and EphB4-His ectodomains. The proteins exhibited complex binding patterns indicating 2:1 heterologous interactions, which is consistent with their known ability to form dimers and tetramers. EphB4 as expected bound only to EphrinB2.

c, BLI studies of SSA sensorchip immobilized biotinylated rat EphB1-Fc, mouse EphB2-Fc, and mouse EphB4-Fc ectodomains binding to 10, 30, and 100 nM soluble mouse EphrinB2-His ectodomain for global fit analysis to accurately determine dissociation constants (K_D) and other kinetic information. As the sensorgram binding traces and curve fits indicate complex associations, 2:1 models were used to calculate two different K_D values, K_{D2} to describe dimer formation and K_{D1} to describe tetramer formation.

d, In a small volume chemiluminescent proximity-based Alpha assay, rat EphB1-Fc ectodomain coated Protein A donor beads were combined with mouse EphrinB2-His ectodomain coated anti-6His acceptor beads and used to screen a 240,000 compound chemical library in 384-well plates.

e, AHC sensorchip immobilized rat EphB1-Fc ectodomain binding to 100 nM soluble mouse EphrinB2-His ectodomain, testing 0, 10, and 100 μM of A20 (2xHCl salt). The sensorgram trace with 100 μM A20 indicates simple 1:1 receptor-ligand binding kinetics, reflecting formation of only the dimer, and the K_D using 1:1 binding model is 46.2 nM.

f, AHC sensorchip immobilized human EphrinB2-Fc ectodomain binding to 50 nM soluble human EphB2-His or EphB4-His ectodomains, testing 0, 1, 10, 100 μM of A20 (2xHCl salt). The large red asterisk indicates strong reduction in the EphrinB2-EphB2 binding response with as little as 1 μM A20, while the small red asterisk indicates little loss of EphrinB2-EphB4 binding with compound addition.
g, AHC immobilized human EphrinB2-Fc ectodomain binding to 100 nM soluble human EphB2-His ectodomain, testing 0, 0.25, 1, 5, 10, 100 μM of peptide SNEW that targets EphB2 or EWLS that targets EphB1. Addition of 100 μM SNEW, but not EWLS, resulted in a reduced slope of response immediately after the start of association step (arrow). A20, which does not alter dimer formation, was also included in the runs at 2 μM as the max control to show much more potent effect of tetramer inhibition on the EphrinB2-EphB2 interaction.
h, Soluble human EphB2-His ectodomain binding to soluble mouse EphrinB2-His ectodomain, testing 0, 10, and 50 μM A20 (2xHCl salt) was assessed using mass photometry. The EphB2-His protein in solution by itself formed a homodimer centered at 130 KDa (the monomer is 70 kDa), and EphrinB2-His protein in solution by itself formed a homodimer centered at 83 KDa (the monomer is 30-40 kDa). When combined, EphB2-His and EphrinB2-His assembled into a tetramer centered at 216 kDa, the size of which shifted to 158 kDa with 10 μM A20 and to 150 kDa with 50 μM A20.
i, A20 contains an 8-hydroxyquinoline (8-HQ) bicyclic heterocyclic scaffold formed by fusion of a phenol ring with a pyridine ring at two adjacent carbon atoms. Medicinal chemistry efforts around the scaffold identified novel analogs with more potent tetramer inhibitor activity, as exemplified by A20-I, 3511-I, and BQPB4, and the schematic summarizes the medicinal chemistry efforts, highlighting the changes that can improve tetramer inhibitor activity (green and purple) and those which result in poor inhibitor activity (yellow) or weak/no activity (red).
j, AHC sensorchip immobilized human EphrinB2-Fc ectodomain binding to 25 nM soluble human EphB2-His ectodomain, testing 0, 0.1, 0.2, 0.4, 0.8, and 1.6 μM of A20 (2xHCl salt) and 0, 0.1, 0.2, 0.4, 0.8, 1.6, and 3.2 μM BQPB4 (free base). Area under the curve (AUC) analysis was used to determine relative IC_{50} and K_i values (shown in red). Relative IC_{50} values were calculated by subtracting the AUC of the max control sensorgram from the AUCs of the concentration-response runs, eliminating the contribution of dimer binding and insurmountable tetramer binding for a more accurate determination of a compound's tetramer inhibitor activity.

Fig. 2. Tetramer inhibitors disrupt EphB2 tyrosine kinase forward signaling in live cells and animals.

a, EphB2 was immunoprecipitated (IP) from protein lysates made from various wild-type (WT) and mutant E14.5 day mouse embryos and subjected to an *in vitro* tyrosine kinase assay by incubating with ATP. The resulting immunoblots (IB) show intracellular juxtamembrane tyrosine residue Y596 of EphB2 becomes autophosphorylated when the catalytic domain is activated by addition of ATP (+) and this results in reduced mobility of ~50% of the protein in SDS-PAGE gels from just under the 130 kDa marker for the unphosphorylated total EphB2 protein to a phosphorylated pEphB2 band just at or above the 130 kDa protein marker only in the WT and F620D catalytic overactive point mutant embryo lysates. The rabbit anti-EphB2 antibody specifiically recognizes the unphosphorylated EphB2 juxtamembrane YIPD sequence, whereas the rabbit anti-pEphB antibody recognizes the same sequence, but only when tyrosine phosphorylated (pYIPD). As expected, the K661R kinase-dead point mutant, knockout (KO), and lacZ intracellular truncated EphB2 mutants did not show a phosphorylation product.

b, Serum-starved Cos1 cells were stimulated for indicated times with soluble EphrinB2-Fc, and resulting protein lysates were mixed with pTyr1000-conjugated sepharose beads to precipitate phosphotyrosine-containing proteins, 100% of which was loaded onto SDS-PAGE gels next to a lane containing 1% of the whole cell lysate collected before pTyr1000 bead addition. After immunoblotting for EphB2, the percent level of pEphB2 (% pEphB2) was quantified for each lysate by dividing the number of phospho-specific pEphB2 photons in the pTyr1000 bead IP lane by the total number of tEphB2 photons using the provided equation. The % pEphB2 (left graph) and fold increase in % EphB2 (right graph) are plotted. The pEphB2 protein species in the pTyr1000 lanes exhibited slightly reduced mobility compared to the unphosphorylated tEphB2 protein in the lysate lanes.

c, Increasing concentrations of EphB2 tyrosine kinase inhibitor MCD were added to serum-starved Cos1 cells grown at high density and stimulated with 1.5 ug/ml (30 nM) pre-clustered EphrinB2-Fc for 32 minutes resulted in a concentration-dependent reduction in the % pEphB2 and when plotted gives an IC_{50} = 121.4 μM. Shown are both composite (to visualize the pre-stained protein standards) and chemiluminescent images of the immunoblot.

d, Increasing concentrations of MCD, A20-I, or BQPB4 were added to serum-starved Cos1 cells plated at low density and stimulated with 1.5 ug/ml (30 nM) unclustered EphrinB2-Fc for 32 minutes resulted in a concentration-dependent reduction in the % pEphB2, with BQPB4 having the strongest effect (IC_{50} = 3.2 μM), followed by A20-I (IC_{50} = 8.5 μM), and then MCD (IC_{50} = 71.2 μM). The IC_{50} values for overall pEphB2 levels were also plotted and shown to be consistent with the % pEphB2 results.
e, In protein lysates made from E14.5 day mouse embryos, activated pEphB2 protein precipitated using various anti-phosphotyrosine antibodies in IP_1 lanes from WT animals exhibits a slightly reduced/slower migration in the gel at or just above the 130 kDa marker compared to the unphosphorylated EphB2 protein in the IP_2 lanes. Based on band intensities, the % pEphB2 present in the embryo is no greater than 1%. No EphB2 protein is detected in the lysates made from knockout (KO) embryos.
f, No pEphB2 protein was detected using anti-phospho-EphB antibodies in IP_1 lanes in lysates made from adult mouse brains, even in the kinase dysregulated F620D mutant, indicating extremely tight negative control over pEphB2 levels in adult tissues.
g, Whole brain protein lysates made from indicated embryonic and postnatal (P) stages showed pEphB2 detected using pTyr1000 + 4G10 Platinum antibodies in IP_1 lanes represented 1.39% of the total EphB2 protein in the E16.5 day embryonic brain, and gradually diminished with age to be almost undetectable by postnatal day 16.
h, Protein lysates from P8 intestines after dosing pups with ~2 ul of a 50 mg/ml solution of A20, EDTA, or vehicle only (100% PBS) showed reduced pEphB2 levels and % pEphB2 in tetramer inhibitor treated animals. Quantification of band intensities and analysis of the % pEphB2 using the equation in **b** revealed A20 treatment led to significantly less % pEphB2, pEphB2 levels, and tEphB2 levels as determined using unpaired t-test. The EDTA treated animals exhibited non-significant trends towards lower % pEphB2, pEphB2 levels, and tEphB2 levels. When combined, significant reductions in % pEphB2 were detected in both the A20 and EDTA dosed animals using one-way analysis of variance (ANOVA) with Dunnett's post-hoc tests. Error bars in all graphs are ± standard error of the mean (± SEM) with significance summaries indicated as: ns non-significant; $^{*}p < 0.05$, $^{**}p < 0.01$, $^{***}p < 0.001$, $^{****}p < 0.0001$. Supplementary Table 3 provides full statistical information for all immunoblot analysis.
i, Protein lysates from P8 kidneys after dosing pups with ~2 ul of a 50 mg/ml solution of A20, EDTA, or vehicle only (100% PBS) showed reduced % pEphB2. Quantification of the band intensities and one-way ANOVA with Dunnett's post-hoc test showed the kidneys from A20 treated mice had a trend towards lower levels of % pEphB2 and that

EDTA treated mice had significantly less % pEphB2, and in both cased there was a highly significant reduction in pEphB2 levels. The tEphB2 levels were not significantly different between the V, A20, and EDTA treated kidneys.

j, Protein lysates from P8 intestines after dosing pups with ~2 ul of a 50 mg/ml solution of A20, EDTA, or vehicle only (100% PBS) showed reduced % pEphB2 detected using SH2 superbinder-conjugated beads in IP lanes. Duplicate lysates of the three A20 and three EDTA treated animals were run on two gels, each with a unique vehicle control. Quantification of the band intensities and one-way ANOVA with Dunnett's post-hoc test analyzing each individual data point (left) or when results of the duplicate samples were averaged (right) revealed that both the A20 and EDTA treated mice had significantly lower % pEphB2 and pEphB2 levels, whereas no significant difference in tEphB2 levels was detected between the three groups.

Fig. 3. Tetramer inhibitors disrupt EphrinB2 reverse signaling in live cells and animals.

a, Phosphotyrosine proteins precipitated from E13.5 embryo lysates using either pTyr1000 conjugated beads or 4G10 antibodies revealed activated pEphrinB2 protein in *EphrinB2* +/+ (WT), but not *EphrinB2* 6YFdV/6YFdV (6YFdV) mutants. The whole embryo lysate lanes show WT and 6YFdV EphrinB2 proteins migrate in SDS-PAGE as a broad band of 35-50 kDa, while the EphrinB2-lacZ/+ heterozygote embryo lysate included in the immunoblot expressed a larger sized, intracellular truncated EphrinB2-βgal fusion protein of ~150 kDa and correspondingly 50% less WT protein and serves as a control for the specificity of the goat anti-EphrinB2 antibody used in the IB. The migration of phosphorylated WT pEphrinB2 protein was slightly retarded in the SDS-PAGE gel compared to the unphosphorylated protein in the lysate lanes.

b, Phosphotyrosine proteins were precipitated from E14.5 embryo lysates using either SH2 superbinder-conjugated beads, pTyr1000 conjugated beads, or 4G10 antibodies revealed activated pEphrinB2 protein in *EphrinB2* +/+ (WT), but not *EphrinB2* lacZ/lacZ (LZ) mutants. The whole embryo lysate lanes (L) show WT EphrinB2 protein migrates in SDS-PAGE as a broad band of 35-50 kDa (red asterisks), while the LZ lysate does not express a WT sized EphrinB2 protein and serves as a control for antibody specificity (dotted red boxes). In the IP lanes, activated, tyrosine phosphorylated pEphrinB2 protein was detected in the WT embryo lysates (green asterisks), whose migration was slightly retarded in the SDS-PAGE gel compared to the unphosphorylated WT protein, while no pEphrinB2 protein was detected in the LZ mutant lysates as expected (dotted

green boxes). The 4G10 IP also identified pEphrinB2 protein (green asterisk), though its signal overlapped with a strong background band corresponding to the 4G10 antibody used in the IP (large yellow asterisks). The antibody background was greatly diminished in the pTyr1000-conjugated bead IPs (small yellow asterisks), and absent in the SH2-bead IPs as no antibody chains are present in this reagent (dotted yellow boxes).
c, BQPB4 added to serum-starved mouse pancreatic stellate cells that were stimulated with 2.5 ug/ml (30 nM) unclustered EphB2-Fc for 60 minutes resulted in a concentration-dependent reduction in the % pEphrinB2. BQPB4 exhibited a strong effect on % pEphrinB2 (IC_{50} = 1.5 μM) and pEphrinB2 levels (IC_{50} = 1.5 μM).
d, EDTA added to serum-starved mouse pancreatic stellate cells that were stimulated with 2.5 ug/ml (30 nM) unclustered EphB2-Fc for 60 minutes resulted in a concentration-dependent reduction in the % pEphrinB2. EDTA exhibited a strong effect on % pEphrinB2 (IC_{50} = 1.1 μM) and pEphrinB2 levels (IC_{50} = 1.9 μM).
e, Intestine lysates prepared from P8 pups after dosing with ~2 ul of a 50 mg/ml solution of EDTA or vehicle only (100% PBS) showed tetramer inhibitor significantly reduced % pEphrinB2 and pEphB2 levels, without affecting tEphrinB2 levels as determined using unpaired t-tests.

Fig. 4. Tetramer inhibitors blunt injury-induced inflammatory pain.
a, General flow of studies to assess ability of tetramer inhibitors to reduce heat and touch pain induced by intraplantar injection of complete freund's adjuvant (CFA) into the left hind paw of mice. For each mouse the uninjured right hind paw response was divided by the injured left hind paw response to obtain a pain ratio which was then plotted and subjected to t-tests, one-way ANOVA, or two-way ANOVA with appropriate post-hoc tests depending on the analysis. Error bars in graphs are ± SEM with significance summaries indicated as: ns non-significant; *$p < 0.05$, **$p < 0.01$, ***$p < 0.001$, ****$p < 0.0001$ (most ns comparisons are omitted from the graphs). Extended Data Fig. 8 and Supplementary Table 3 provide full statistical information for all pain studies.
b,c, Thermal (**b**) and mechanical (**c**) pain ratios obtained on multiple days from a group of CFA-injured littermate-matched *EphB1* +/+ wild-type (WT), -/- knockout (KO), and lacZ/lacZ intracellular truncated (LZ) homozygous mutant mice.
d-f, Thermal pain ratios from obtained +3 days post-CFA on different groups of WT mice that assessed i.p. injection of: (**d**) vehicle only, A20 free base (20 mg/kg), MCD kinase inhibitor (10 mg/kg), or dual injected with both A20+MCD, (**e**) vehicle only, A20

salt (20 mg/kg), or QPB4-Bn salt (20 mg/kg), (**f**) vehicle only, QPB4 salt (20 mg/kg), or QPP-127 salt (20 mg/kg).

g,h, Thermal (**g**) and mechanical (**h**) pain ratios obtained on multiple days from a group of WT mice that were either oral gavaged with vehicle only, i.p. injected with A20 salt (20 mg/kg), or oral gavaged with A20 salt (20 mg/kg) and assessed for thermal/ mechanical pain following the schedule outlined in (**a**).

i, Thermal and mechanical pain measurements and pain ratios obtained from a group of Zymosan-injured littermate-matched *EphB1* +/+ (WT), -/- (KO), and +/- (heterozygote) mice.

j, Mechanical pain measurements and pain ratios obtained from a group of Zymosan-injured littermate-matched *EphrinB2* +/+ (WT) and *EphrinB2* lacZ/6YFdV reverse signaling deficient mice.

k, Thermal and mechanical pain measurements and pain ratios obtained from a group of Zymosan-injured WT mice that were orally dosed 15 minutes post-Zymosan with either vehicle only, or with 3511-I salt (20 mg/kg) or BQPB4 salt (20 mg/kg). Two hours after Zymosan injection, the injured left hind paws were assessed for mechanical pain (2-4 hr), then mice were orally dosed again with vehicle only or 3511-I/BQPB4 compounds, and then hind paws tested for thermal pain (4-6 hr), and again for mechanical pain (6-8 hr).

l, Thermal pain measurements and pain ratios obtained from a group of Zymosan-injured WT mice that were orally dosed 15 minutes post-Zymosan with either vehicle only, or with 5, 10, or 20 mg/kg of BQPB4 salt. Two hours after Zymosan injection, the hind paws were assessed for mechanical pain (2-4 hr), then mice were orally dosed again with vehicle only or BQPB4, and then hind paws tested for thermal pain (4-6 hr), and again for mechanical pain (6-8 hr). Shown are the thermal pain results.

Fig. 5. A20 blunts dorsal horn (DH) neuron activation in the spinal cord after injury-induced inflammatory pain.

a, Representative images of red fluorescent DH neurons in the lumbar spinal cord from a group of 20 week old female *EphB1*+/+ (WT), +/- (HET), and -/- (KO) mice that also contained the *Trap2-CreERT2* driver and the *Ai9-tdTomato* reporter. Animals were injected with CFA into their left hind paw to induce inflammatory pain and 4 hr later injected i.p. with 4-hydroxytamoxifen (4-OHT) to activate Cre recombinase and permanently label with red fluorescence the neurons that were activated. Two weeks later, spinal cords were perfusion fixed and serial sections (50 μm) through the lumbar

spinal cord were obtained with a vibratome and red fluorescent neurons imaged and counted on the left (injured) and right (uninjured) side dorsal horns (boxed areas) from 8-12 sections. The ratio of Trap2+ activated neurons for each animal was determined by dividing the average number of red neurons from the injured side by the number obtained from the uninjured side. One-way ANOVA analysis revealed significantly reduced DH neuron ratios in the +/- and -/- animals compared to +/+.

b, Representative images of red fluorescent DH neurons in the lumbar spinal cord from a group of CFA-injured WT mice that were treated with i.p. injection of either vehicle or 20 mg/kg A20 (3%DMSO/97%PBS), or 10 mg/kg MCD (100% PBS). The ratio of left/right red neurons for each mouse was determined from 8-12 serial 50 μm sections along the span of the lumbar cord. Similar to the +/+ controls in **a**, the DH neurons in the left-injured side of vehicle treated mice showed ~3 times more Trap2/tdTomato red fluorescent labeled neurons compared to the uninjured right side, whereas A20 treated mice had significantly fewer labeled neurons in the injured side with a ratio ~1.5.

Fig. 6. A20 blunts opioid withdrawal behaviors.

a, A group of eight month old male *EphB1* +/+ *and* -/- littermates were given nine escalating doses of morphine over a 96 hr period, and then 3 hr after final morphine dose were injected subcutaneously with naloxone hydrochloride to precipitate withdrawal. Animals were monitored for 30 min and the number of jumps plotted as an indicator of withdrawal intensity, with t-test indicating the WT mice exhibited significantly more jumps than the knockouts lacking expression of the EphB1 receptor.

b, Shown are pooled results plotting the number of jumps from two different opioid withdrawal experiments comparing vehicle to A20 dosed mice (a total of seven IP injections of V or A20, from 24-96 hr), one using CD1 strain mice (2 mice V and 3 mice A20) and the other using C57BL/6 strain mice (3 mice V and 4 mice A20). A t-test indicates the V mice exhibited significantly more jumps than the A20 treated animals.

c, Shown are the incidence of diarrhea, tremor, and ptosis that were scored during the withdrawal study using C57BL/6 strain mice in **b**.

d, Schematic summarizing how tetramer inhibitors block EphB-EphrinB2 forward and reverse signaling to blunt pain and addiction.

Figure 1

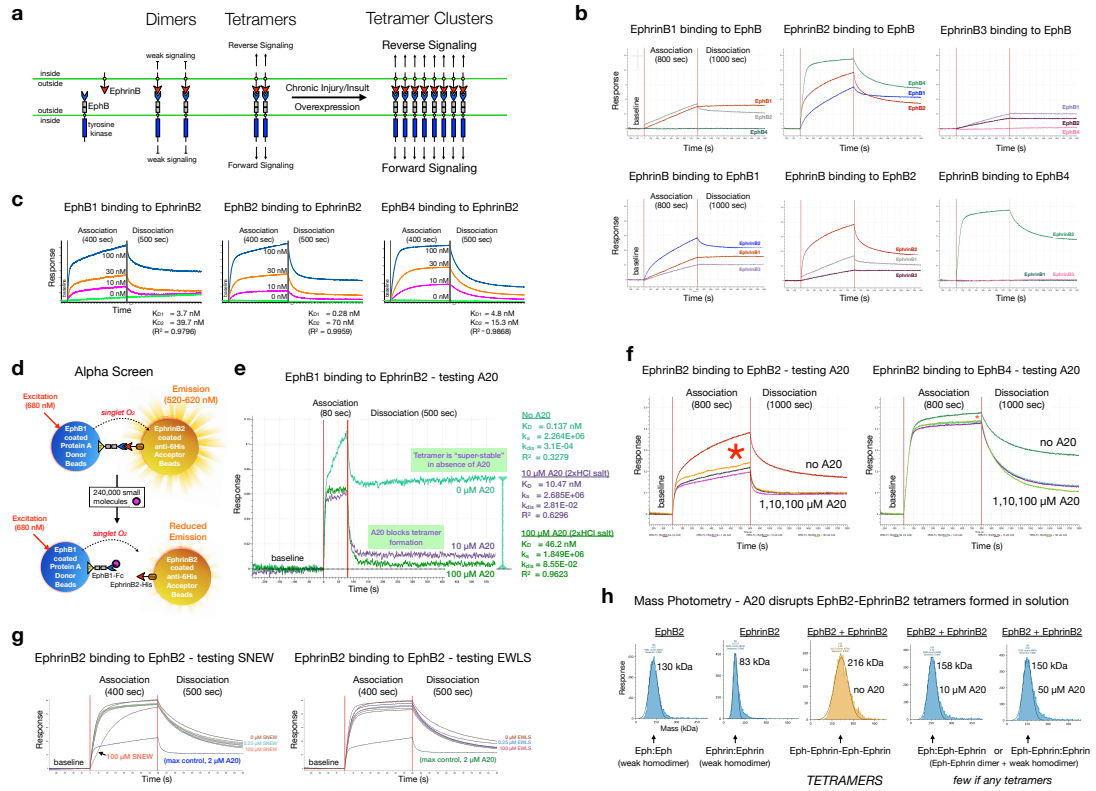
a
Dimers
Tetramers
Tetramer Clusters
weak signaling
Reverse Signaling
Reverse Signaling
inside
outside
EphrinB
EphB
outside
inside
tyrosine kinase
Chronic Injury/Insult
Overexpression
weak signaling
Forward Signaling
Forward Signaling
b
EphrinB1 binding to EphB
EphrinB2 binding to EphB
EphrinB3 binding to EphB
Association (800 sec)
Dissociation (1000 sec)
Response
baseline
Time (s)
EphrinB binding to EphB1
EphrinB binding to EphB2
EphrinB binding to EphB4
c
EphB1 binding to EphrinB2
EphB2 binding to EphrinB2
EphB4 binding to EphrinB2
Association (400 sec)
Dissociation (500 sec)
100 nM
30 nM
10 nM
0 nM
Response
Time
KD1 = 3.7 nM
KD2 = 39.7 nM
(R² = 0.9796)
KD1 = 0.28 nM
KD2 = 70 nM
(R² = 0.9959)
KD1 = 4.8 nM
KD2 = 15.3 nM
(R² = 0.9868)
d
Alpha Screen
Excitation (680 nM)
Emission (520-620 nM)
singlet O₂
EphB1 coated Protein A Donor Beads
EphrinB2 coated anti-6His Acceptor Beads
240,000 small molecules
Excitation (680 nM)
singlet O₂
Reduced Emission
EphB1 coated Protein A Donor Beads
EphB1-Fc
EphrinB2-His
EphrinB2 coated anti-6His Acceptor Beads
e
EphB1 binding to EphrinB2 - testing A20
Association (80 sec)
Dissociation (500 sec)
Response
baseline
Tetramer is "super-stable" in absence of A20
0 μM A20
A20 blocks tetramer formation
10 μM A20
100 μM A20
Time (s)
No A20
KD = 0.137 nM
ka = 2.264E+06
kdis = 3.1E-04
R² = 0.3279
10 μM A20 (2xHCl salt)
KD = 10.47 nM
ka = 2.685E+06
kdis = 2.81E-02
R² = 0.6296
100 μM A20 (2xHCl salt)
KD = 46.2 nM
ka = 1.849E+06
kdis = 8.55E-02
R² = 0.9623
f
EphrinB2 binding to EphB2 - testing A20
EphrinB2 binding to EphB4 - testing A20
Association (800 sec)
Dissociation (1000 sec)
Response
baseline
no A20
1,10,100 μM A20
Time (s)
g
EphrinB2 binding to EphB2 - testing SNEW
EphrinB2 binding to EphB2 - testing EWLS
Association (400 sec)
Dissociation (500 sec)
Response
baseline
100 μM SNEW
(max control, 2 μM A20)
Time (s)
h
Mass Photometry - A20 disrupts EphB2-EphrinB2 tetramers formed in solution
EphB2
EphrinB2
EphB2 + EphrinB2
EphB2 + EphrinB2
EphB2 + EphrinB2
Response
Mass (kDa)
130 kDa
83 kDa
216 kDa
no A20
158 kDa
10 μM A20
150 kDa
50 μM A20
Eph:Eph (weak homodimer)
Ephrin:Ephrin (weak homodimer)
Eph-Ephrin-Eph-Ephrin
Eph:Eph-Ephrin or Eph-Ephrin:Ephrin (Eph-Ephrin dimer + weak homodimer)
TETRAMERS
few if any tetramers
i
Medicinal chemistry around the A20 scaffold
8-HQ
A20
A20-I
3511-I
BQPB4
j
EphrinB2 binding to EphB2 - testing A20
EphrinB2 binding to EphB2 - testing BQPB4
Association (400 sec)
Dissociation (500 sec)
A20
IC50 = 0.48 μM
Ki = 5.32 nM
BQPB4
IC50 = 0.26 μM
Ki = 2.88 nM
Response
baseline
(max control)
Time (s)

Figure 2

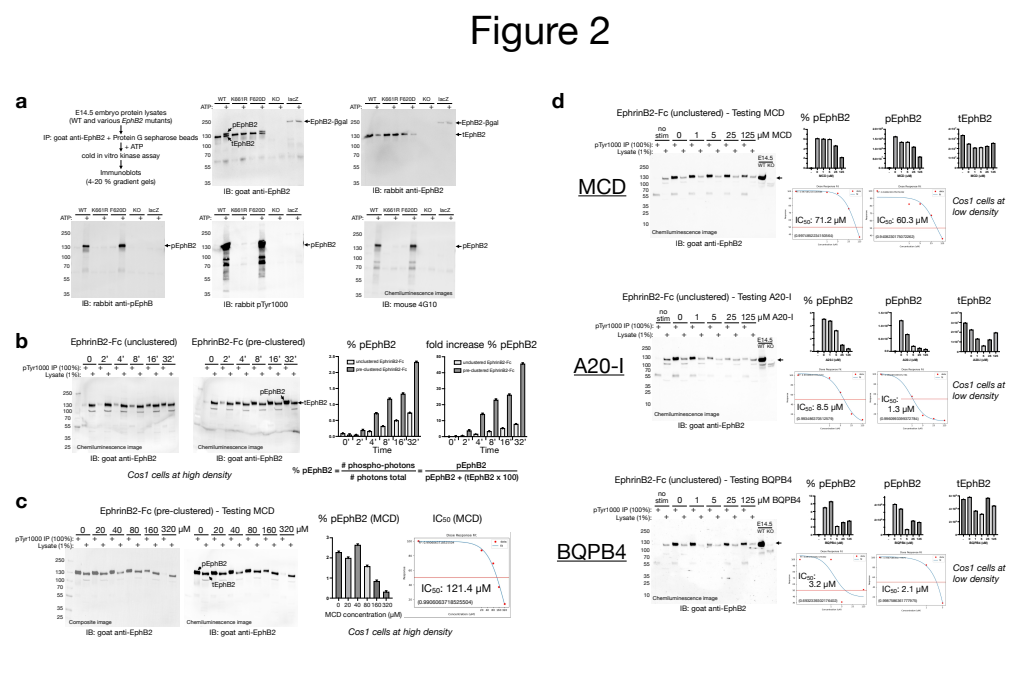
a
E14.5 embryo protein lysates (WT and various EphB2 mutants)
IP: goat anti-EphB2 + Protein G sepharose beads
+ ATP
cold in vitro kinase assay
Immunoblots (4-20 % gradient gels)
WT K661R F620D KO lacZ
ATP
pEphB2
tEphB2
EphB2-βgal
IB: goat anti-EphB2
IB: rabbit anti-EphB2
IB: rabbit anti-pEphB
IB: rabbit pTyr1000
IB: mouse 4G10
Chemiluminescence images
b
EphrinB2-Fc (unclustered)
EphrinB2-Fc (pre-clustered)
pTyr1000 IP (100%):
Lysate (1%):
0 2' 4' 8' 16' 32'
Chemiluminescence image
IB: goat anti-EphB2
Cos1 cells at high density
% pEphB2
fold increase % pEphB2
unclustered EphrinB2-Fc
pre-clustered EphrinB2-Fc
Time
% pEphB2 = # phospho-photons / # photons total = pEphB2 / pEphB2 + (tEphB2 x 100)
c
EphrinB2-Fc (pre-clustered) - Testing MCD
0 20 40 80 160 320 μM
Composite image
% pEphB2 (MCD)
IC50 (MCD)
MCD concentration (μM)
IC50: 121.4 μM
d
MCD
EphrinB2-Fc (unclustered) - Testing MCD
no stim 0 1 5 25 125 μM MCD
E14.5 WT KO
% pEphB2
pEphB2
tEphB2
IC50: 71.2 μM
IC50: 60.3 μM
Cos1 cells at low density
A20-I
EphrinB2-Fc (unclustered) - Testing A20-I
no stim 0 1 5 25 125 μM A20-I
IC50: 8.5 μM
IC50: 1.3 μM
BQBP4
EphrinB2-Fc (unclustered) - Testing BQBP4
no stim 0 1 5 25 125 μM BQBP4
IC50: 3.2 μM
IC50: 2.1 μM

Figure 2 (continued)

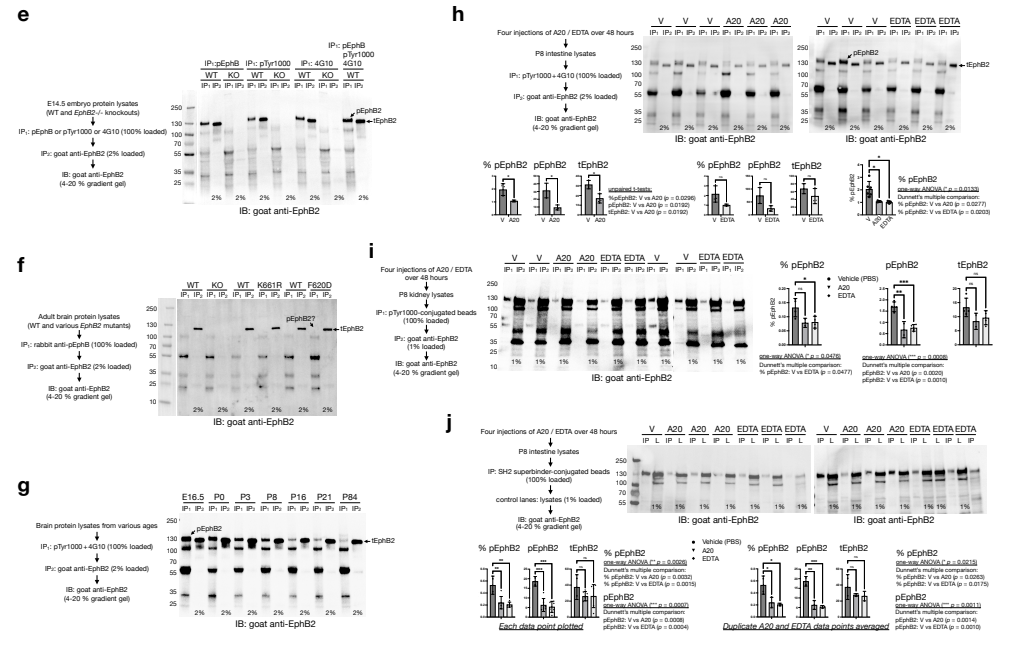

Figure 3

a

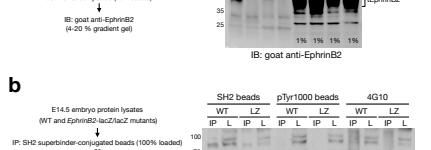

b

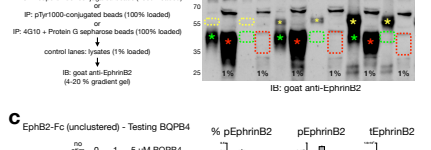

c

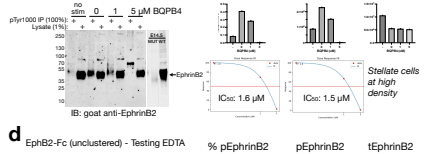

d

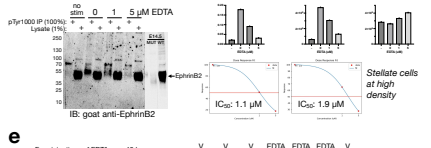

e

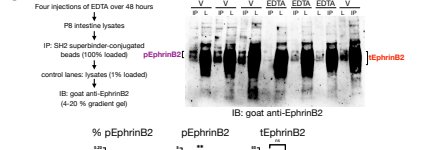

Figure 4

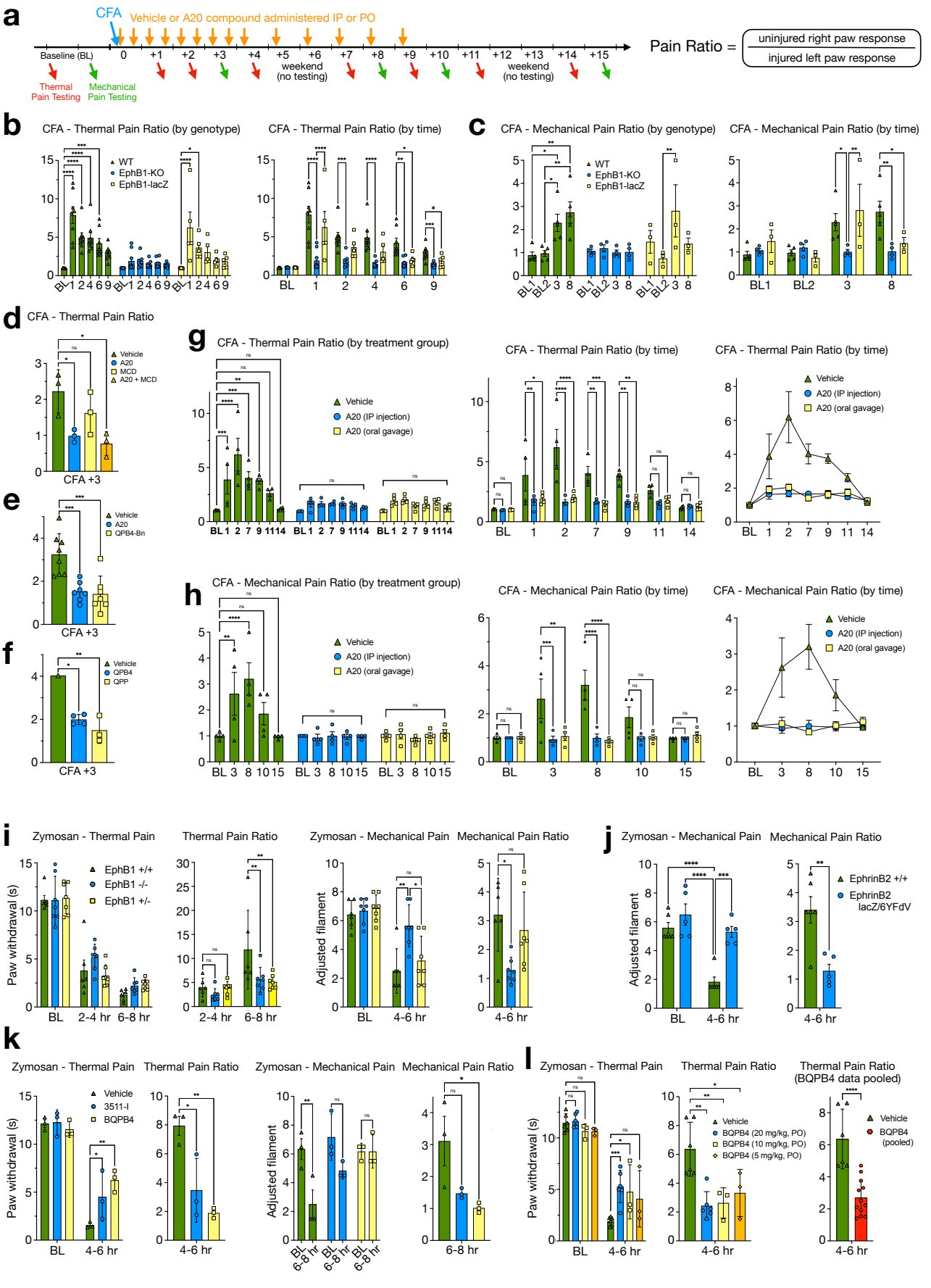
a
CFA
Vehicle or A20 compound administered IP or PO
Baseline (BL)
0 +1 +2 +3 +4 +5 +6 +7 +8 +9 +10 +11 +12 +13 +14 +15
weekend (no testing)
weekend (no testing)
Thermal Pain Testing
Mechanical Pain Testing
Pain Ratio = uninjured right paw response / injured left paw response
b
CFA - Thermal Pain Ratio (by genotype)
CFA - Thermal Pain Ratio (by time)
WT
EphB1-KO
EphB1-lacZ
c
CFA - Mechanical Pain Ratio (by genotype)
CFA - Mechanical Pain Ratio (by time)
d
CFA - Thermal Pain Ratio
Vehicle
A20
MCD
A20 + MCD
CFA +3
e
Vehicle
A20
QPB4-Bn
CFA +3
f
Vehicle
QPB4
QPP
CFA +3
g
CFA - Thermal Pain Ratio (by treatment group)
CFA - Thermal Pain Ratio (by time)
CFA - Thermal Pain Ratio (by time)
Vehicle
A20 (IP injection)
A20 (oral gavage)
h
CFA - Mechanical Pain Ratio (by treatment group)
CFA - Mechanical Pain Ratio (by time)
CFA - Mechanical Pain Ratio (by time)
i
Zymosan - Thermal Pain
Thermal Pain Ratio
Zymosan - Mechanical Pain
Mechanical Pain Ratio
EphB1 +/+
EphB1 -/-
EphB1 +/-
Paw withdrawal (s)
Adjusted filament
j
Zymosan - Mechanical Pain
Mechanical Pain Ratio
EphrinB2 +/+
EphrinB2 lacZ/6YFdV
k
Zymosan - Thermal Pain
Thermal Pain Ratio
Zymosan - Mechanical Pain
Mechanical Pain Ratio
Vehicle
3511-I
BQPB4
l
Zymosan - Thermal Pain
Thermal Pain Ratio
Thermal Pain Ratio (BQPB4 data pooled)
BQPB4 (20 mg/kg, PO)
BQPB4 (10 mg/kg, PO)
BQPB4 (5 mg/kg, PO)
BQPB4 (pooled)

Figure 5

a

left (injured) right (uninjured)

+/+

+/-

-/-

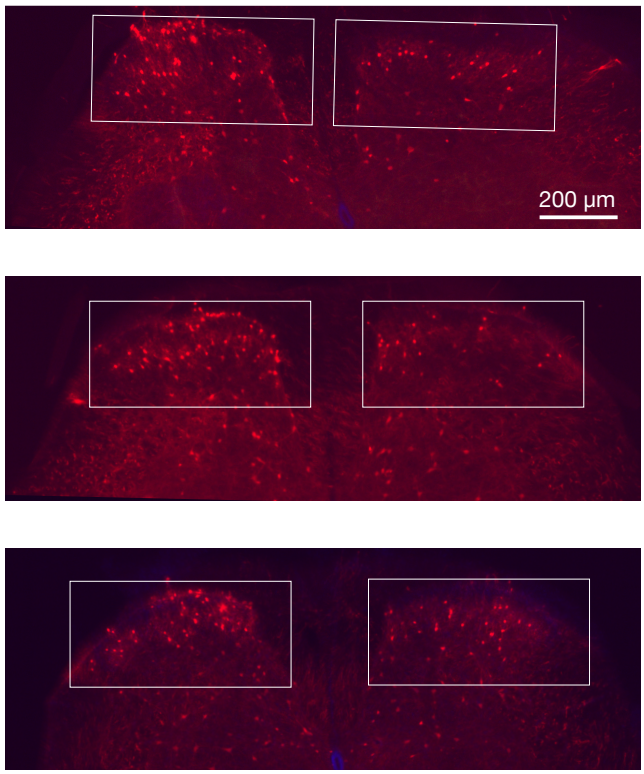

Ratio of Trap2+ DH neurons

red neurons (injured side) / red neurons (uninjured side)

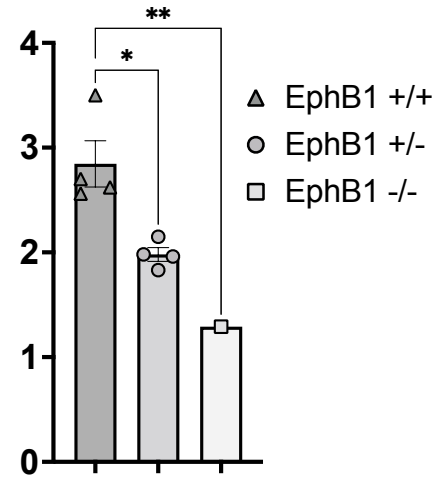

one-way ANOVA (** p = 0.0074)
Dunnett's multiple comparison:
+/+ vs +/- (p = 0.0173)
+/+ vs -/- (p = 0.0097)

b

left (injured) right (uninjured)

Vehicle

A20

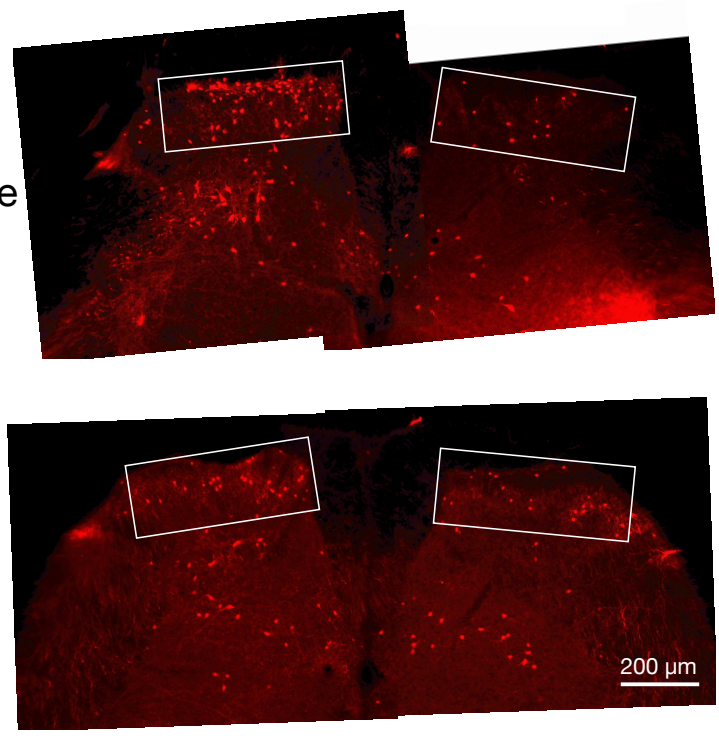

Ratio of Trap2+ DH neurons

red neurons (injured side) / red neurons (uninjured side)

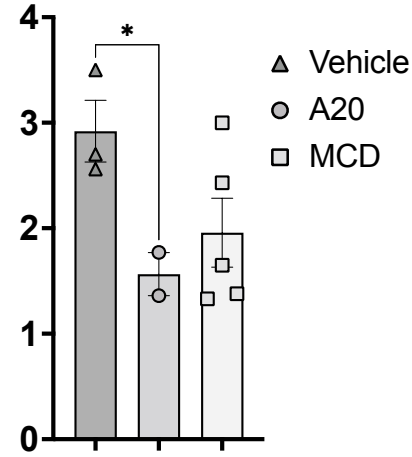

one-way ANOVA
Šídák's multiple comparisons test:
V vs A20 (p = 0.0491)
unpaired t-test: p = 0.0322

Figure 6

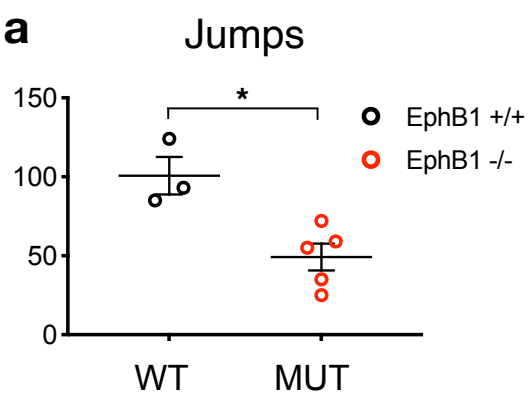

unpaired t-test: $p = 0.0112$

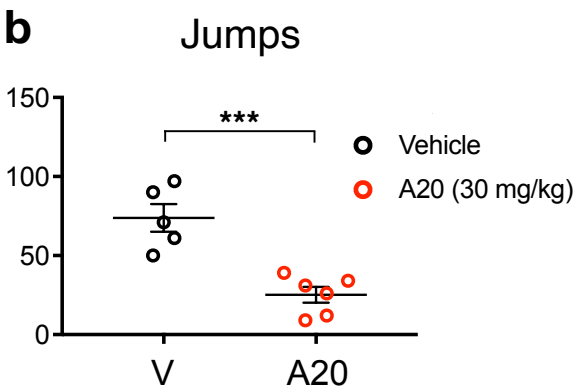

unpaired t-test: $p = 0.0007$

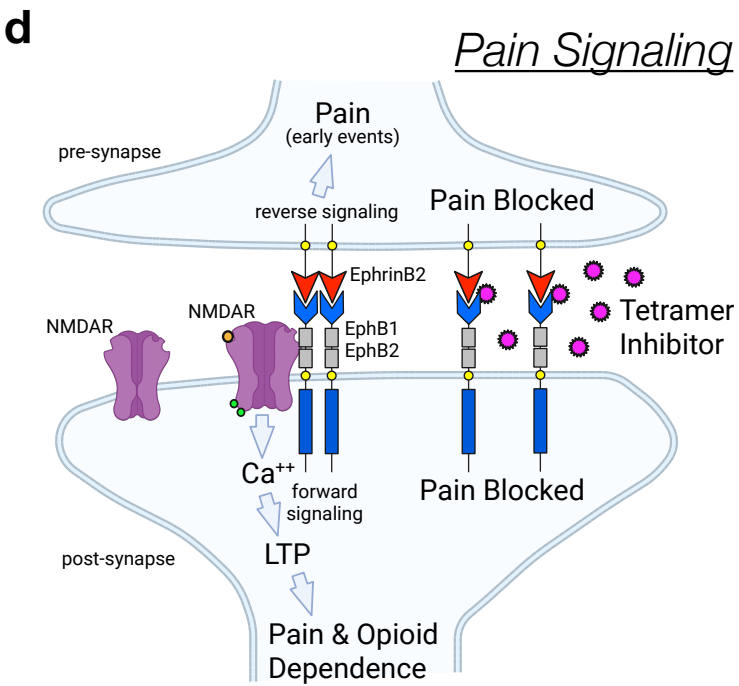

c

Diarrhea	V	= 2 of 3 showed diarrhea
	A20	= 0 of 4 showed diarrhea
Tremor	V	= 6/18 = 33.3% of the time showed tremor
	A20	= 4/24 = 16.7% of the time showed tremor
Ptosis	V	= 4/18 = 22.2 % of the time showed ptosis
	A20	= 0/24 = 0.0 % of the time showed ptosis